Levitated Nanoparticle Photon Scattering

Swansea University
Department of Physics
College of Science

Rafal Gajewski

May 2020

Swansea University
Prifysgol Abertawe

Contents

1 Abstract

Using a fibre-transmitted 1550nm laser, passed through a high NA aspheric lens, a nanoparticle of silica was trapped in the focus of the laser field by optical forces. For this purpose an optical fibre system was constructed, and different arrangements were tested. Experiments were conducted at ambient pressure and in a high vacuum environment, at room temperature. The experiment gave access to an interferometric signal, analysis of which produced characteristic power spectral densities corresponding to those pressure regimes. Based on the information gained from observing Rayleigh scattered light, a proof-of-principle experimental technique was developed in a simulation to be used in trapping experiments, for transferring the particle between intensity maxima of a standing wave. The technique relies on the application of the Unscented Kalman filter, used to accurately infer the position and velocity of the particle in real-time during trapping. Through inference, the scheme was used to successfully transfer the simulated particle in a desired direction with 62%-96% accuracy. Successful experimental implementation of the technique can aid to suppress Radiation Pressure Shot Noise (RPSN) which is a fundamental limitation to achievable sensitivity in levitated particle experiments. The flaws and potential improvements to the technique were also discussed.

2 Introduction

2.1 Motivation

After its experimental confirmation in 1901 [1], the question remained whether radiation pressure can be utilised for practical applications. The original prediction by Maxwell indicated that the optical forces generated by conventionally available sources would be small, therefore hard to measure in the background of thermal fluctuations, and essentially only effective on an astronomical scale [1]. However, further theoretical developments [2] and technological advancements of the 20^{th} century allowed researchers to exploit these forces to gain a high degree of control over individual dielectric particles and even atoms [3]. The development of lasers and high vacuum pumps enabled access to greater intensities and reduced disturbances from the environment, crucial for precise particle manipulation. This gave rise to the first series of practical applications in metrology, sensing, study of light scattering and cloud physics processes [3, 4] and the laser cooling of atoms. Cooling using radiation pressure was also investigated for objects on the micro-scale [5] along with measurement of weak forces [6]. This spurred interest in using radiation pressure for precise measurements, particularly detection of gravitational waves. Two decades later, Braginsky had also established a fundamental limit on measurement of small forces, influencing the realisation of the LIGO project [7]. After the first successful demonstration of optical feedback cooling for a macroscopic mirror [8], due to advancements in microfabrication kelvin and subkelvin temperatures were reached [9] (see figure 2.1), many deviating from the original microcantilever coupling design [10–12].

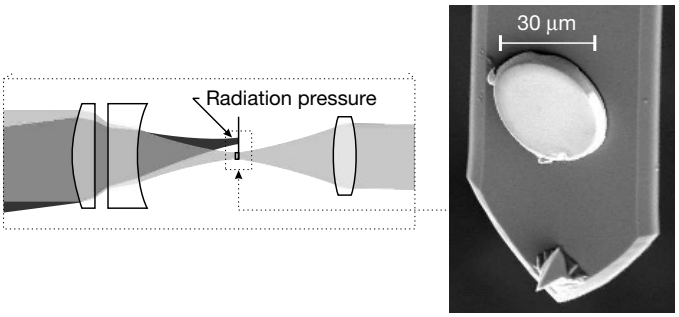

Figure 2.1: Cavity designed to cool a micromechanical resonator to subkelvin temperatures by optical feedback [9]. Scanning electron microscope image of the tip of the cantilever with a micromirror attached (adapted from [9]) is shown on the right. Light transmitted through the cavity (light gray beam) allows to infer the velocity of the cantilever. This information allows to modulate the optical feedback (dark gray beam), which is directed to exert radiation pressure on the cantilever, thereby cooling the resonator.

Aside from its potential in sensing and metrology, cavity optomechanics is proposed to serve as a platform to create quantum superpositions of macroscopic objects [13, 14] to explore the boundary

between quantum and classical physics. One example application is probing fundamental problems such as the existence of exotic decoherence effects [14]. However, optomechanical systems which are mechanically coupled permit heat leakage between components of that system. This is not desired, since heat leakage is a thermal decoherence process which may swamp the underlying dynamics, which are the primary focus of study in these systems. This *clamping* effect can be avoided by making the area of contact as small as possible or by cryogenic cooling [7]. Levitated optomechanics offers a promising route for exploration of the dynamics of objects on the mesoscopic scale, while eliminating the detrimental limitations to the achievable centre of mass temperatures [15, 16]. A nanoparticle trapped in a laser beam is mechanically disconnected from the environment such that the clamping effect is not present. The proposed scheme [17] was realised [18], displayed nano-scale control over the position, and proven to be successful in cooling down to the quantum mechanical ground state of a mechanical mode [19, 20] and force detection with 10^{-21}N sensitivity [21]. Elimination of clamping means that much greater Q-factors can be reached without the need of cryogenic cooling. [15].

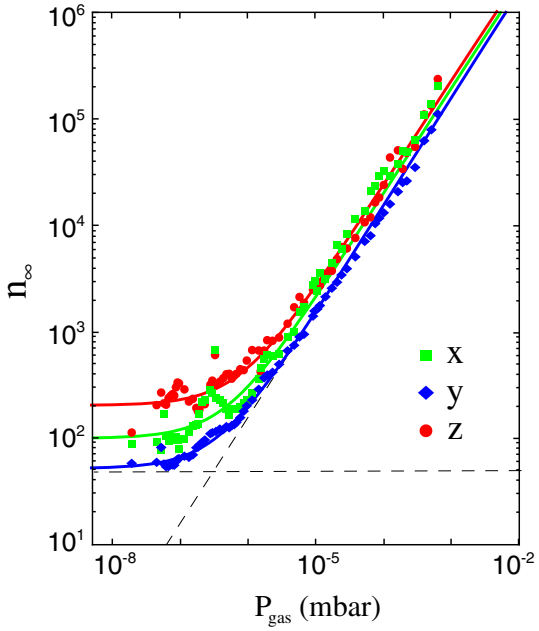

Figure 2.2: First observation of RPSN in a levitated nanoparticle experiment, adapted from [22]. Steady-state mean occupation number. vs. environment pressure. n_∞ decreases with gas pressure until the effect saturates due to RPSN.

Although not clamped, levitated nanoparticles are coupled to the molecules of gas in the environment which supply random momentum kicks to the nanoparticle. This effect limits achievable phonon occupation number (or temperature), but can be mitigated by evacuating the system. Lowering the damping rate due to the finite pressure of the surrounding gas reveals another limiting process in the system due to the trapping laser beam; the particle suffers from random

momentum kicks provided by the Rayleigh scattered light, which is apparent at very low pressures (see figure 2.2). Increasing number of incident photons N to decrease the position uncertainty of a trapped object $\Delta x = 1/(2k\sqrt{N})$ is counteracted by the disturbing effect of photon recoil heating. As a consequence, this radiation pressure shot noise (RPSN) is always present in levitated optomechanical systems and at low pressures dominates as the main limiting factor to lowering the phonon occupation number [22].

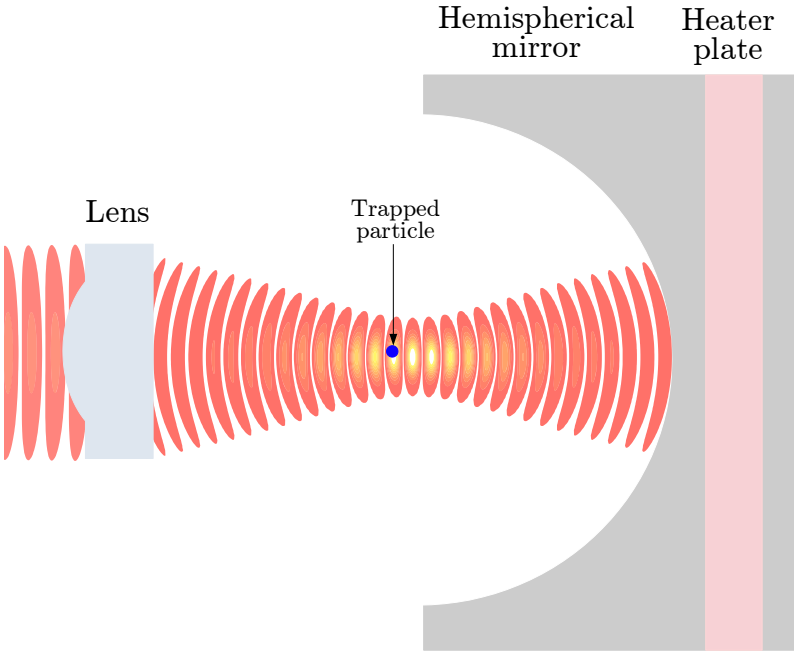

Figure 2.3: Optical arrangement which could be used to suppress RPSN. A nanoparticle is trapped near a maximum of intensity of a standing wave formed between a focusing lens and a reflective hemispherical mirror. A heater plate placed behind the mirror could be used to uniformly heat the mirror and hence be a able to have wavelength-scale control over its radius.

The objective of this Master's project was a mixture of experimental, computational and theoretical work that will ultimately aid the realisation of a novel scheme of suppression of RPSN from Rayleigh scattering. The scheme intends to utilise a hemispherical mirror to suppress the disruptive Rayleigh scattered light at its geometric focus by destructive interference (see figure 2.3). If the optics are aligned for retro-reflection, the retro-reflected light arriving at the geometric focus would interfere constructively or destructively, as proven to provide enhancement as a classical interference effect [23]. In order to yield cancellation of scattered light, the mirror is required to have a radius size close to an integer number of wavelengths. The heater plate can be used to finely tune mirror radius to ensure destructive interference. In the tuning process, it would be expected to see a periodic enhancement and suppression of Rayleigh scattered light

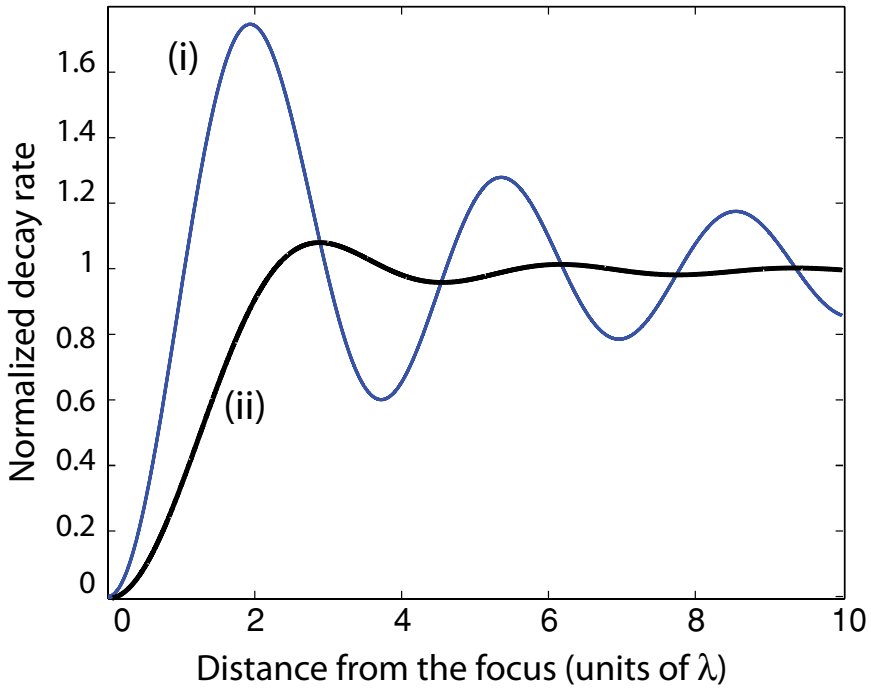

Figure 2.4: A theoretical result adapted from [24] as a result of a QED calculation. The graph shows spontaneous decay rate as a function of displacement of an atom from the centre of a hemispherical mirror in units of wavelength. The two curves correspond to (i) displacement along the mirror axis and (ii) perpendicular to mirror axis.

constrained by a hemispherical mirror, [24] similarly to the theoretical result shown in figure (2.4).

As part of the project, an experiment was built which was used to trap and manipulate a nanoparticle of fused silica in ultrahigh vacuum, gathering a phase sensitive interferometric signal used to infer particle's position. Throughout the run of the project, a range of focusing objectives and optical arrangements were considered and tested, on both sides of the paraxial approximation regime. Once optically aligned, the beam forms a standing wave between the focusing objective and the hemispherical mirror. One of the problems which arise when considering RPSN suppression in this scheme is that the nanoparticle may be trapped at a maximum too far from the geometric focus for the Rayleigh scatter suppression to occur. Computationally, the idea of stimulating the nanoparticle to hop between standing wave maxima in controlled fashion was explored by means of a simulation. By manipulating the intensity amplitude of the laser beam, the particle can be made to transfer ballistically by parametric excitation.

3 Background

This section focuses on developing all the necessary theoretical tools that were used to obtain all experimental and computational results. Starting with the Gaussian model of a laser beam and its properties in section 3.1, the section briefly explains how trapping with optical forces is achieved in 3.3, and the resulting particle dynamics in 3.4. The power spectral density is introduced in section 3.5 as a tool of extracting useful information out of a time sequence. The section ends with the theoretical background of the standard Kalman filter in 3.6 and motivation behind using the Unscented Kalman filter in 3.7.

3.1 Gaussian Optics

The Gaussian beam is the lowest order mode solution to the wave equation when considered under the paraxial approximation.[1] It is a particularly useful description when considering output of laser beams which, due to the spatial extent of lasers' resonator cavities, usually output only the lowest order mode.

Starting from the spatial part of the wave equation,

$$(\nabla^2 + k^2)\widetilde{E}(\vec{\mathbf{r}}) = 0, \tag{3.1}$$

where $\widetilde{E}(\vec{\mathbf{r}})$ is the complex amplitude of the field distribution, $\vec{\mathbf{r}} = (x, y, z)$ is some observation point, and k is the wave number. Considering a beam propagating in the z direction with wavelength λ with small variation in the transverse direction,[2]

$$\widetilde{E}(\vec{\mathbf{r}}) \equiv E_0 \widetilde{u}(\vec{\mathbf{r}}) e^{-ikz}, \tag{3.2}$$

where $\widetilde{u}(\vec{\mathbf{r}})$ is a scalar function that changes slowly in z. More rigorously, we require that $\widetilde{u}(\vec{\mathbf{r}})$

[1] Alternatively, the Gaussian beam can be obtained by considering the Huygens' integral under the Fresnel approximation

[2] this in part, is the paraxial approximation

satisfies,

$$\left|\frac{\partial^2 \widetilde{u}(\vec{\mathbf{r}})}{\partial z^2}\right| \ll \left|2k\frac{\partial \widetilde{u}(\vec{\mathbf{r}})}{\partial z}\right|$$

$$\left|\frac{\partial^2 \widetilde{u}(\vec{\mathbf{r}})}{\partial z^2}\right| \ll \left|\frac{\partial^2 \widetilde{u}(\vec{\mathbf{r}})}{\partial x^2}\right| \tag{3.3}$$

$$\left|\frac{\partial^2 \widetilde{u}(\vec{\mathbf{r}})}{\partial z^2}\right| \ll \left|\frac{\partial^2 \widetilde{u}(\vec{\mathbf{r}})}{\partial y^2}\right|$$

Substituting into (3.1) gives,

$$\nabla^2 \widetilde{u}(\vec{\mathbf{r}}) - 2ik\frac{\partial \widetilde{u}(\vec{\mathbf{r}})}{\partial z} = 0, \tag{3.4}$$

and using (3.3) to drop the second derivative in z to get the *paraxial Helmholtz equation*,

$$\left(\frac{\partial^2}{\partial x^2} + \frac{\partial^2}{\partial x^2} - 2ik\frac{\partial}{\partial z}\right)\widetilde{u}(\vec{\mathbf{r}}). \tag{3.5}$$

Now considering an ansatz of the form, [25]

$$\widetilde{u}(\vec{\mathbf{r}}) = A(z)\exp\left[-ik\frac{x^2+y^2}{2\widetilde{q}(z)}\right], \tag{3.6}$$

where $\widetilde{q}(z)$ is complex function of z, and upon substitution into (3.5) yields the equation,

$$\left[\left(\frac{k}{2}\right)^2\left(\frac{\mathrm{d}\widetilde{q}(z)}{\mathrm{d}z} - 1\right) - \frac{2ik}{\widetilde{q}}\left(\frac{\widetilde{q}}{A(z)}\frac{\mathrm{d}A(z)}{\mathrm{d}z} + 1\right)\right]A(z) = 0. \tag{3.7}$$

A non-trivial solution is found when,

$$\frac{\mathrm{d}\widetilde{q}}{\mathrm{d}z} = 1,$$

$$\frac{\mathrm{d}A(z)}{\mathrm{d}z} = \frac{A(z)}{\widetilde{q}(z)}, \tag{3.8}$$

solved by,

$$\widetilde{q}(z) = \widetilde{q}_0 + z - z_0,$$

$$\frac{A(z)}{A_0} = \frac{\widetilde{q}_0}{\widetilde{q}(z)}. \tag{3.9}$$

Conventionally, a choice is made for the parameters in (3.9),

$$\begin{aligned} A_0 &= i \\ \widetilde{q_0} &= z_R = \frac{n\pi\omega(z)^2}{\lambda} \end{aligned} \tag{3.10}$$

which conveniently redefine equation (3.6) in terms of quantities widely used to characterise Gaussian beams. In equation (3.10), n is the index of refraction of the propagation medium and $\omega(z)^2$ will later be identified as the beam spot size. A_0 was set equal to i as a global phase shift to the solution, ensuring that the curvature of the wavefronts $R = \infty$ at the *beam waist* [26]. With this choice made, the factor of $1/\widetilde{q}(z)$ inside the exponential of equation (3.6) becomes,

$$\begin{aligned} \frac{1}{\widetilde{q}(z)} &= \frac{1}{z + iz_R} \\ &= \frac{z - iz_R}{z^2 + z_R^2} \\ &= \frac{1}{R(z)} - i\frac{\lambda}{n\pi\omega(z)^2}. \end{aligned} \tag{3.11}$$

The pre-factor of equation (3.6) can be equivalently expressed in terms of the amplitude and phase, [25, 26]

$$\frac{i\widetilde{q_0}}{\widetilde{q}(z)} = \frac{\omega_0}{\omega(z)}\exp(i\psi(z)) \tag{3.12}$$

then substituting (3.11) and (3.12) into (3.6), it can be recovered to its more familiar form,

$$\widetilde{E}(r,z) = E_0\widetilde{u}(r,z)e^{ikz} = E_0\frac{\omega_0}{\omega(z)}\exp\left(-\frac{r^2}{\omega(z)^2}\right)\exp\left(-i\left[kz + k\frac{r^2}{2R(z)} - \psi(z)\right]\right), \tag{3.13}$$

for $r^2 = x^2 + y^2$. This particular solution to the paraxial wave equation comes with three key results which characterise the Gaussian beam,

$$\begin{aligned} \omega(z) &= \omega_0\sqrt{1 + \left(\frac{z}{z_R}\right)^2} && \text{Beam width} \\ R(z) &= z\sqrt{1 + \left(\frac{z_R}{z}\right)^2} && \text{Radius of curvature} \\ \psi(z) &= \arctan\left(\frac{z}{z_R}\right) && \text{Gouy phase} \end{aligned} \tag{3.14}$$

From figure (3.1) it can be seen that for large focal length f (or equivalently large z_R), the following relationship can be established,

$$\frac{d}{2f} \approx \frac{\sqrt{2}w_0}{z_R} = \frac{\sqrt{2}\lambda}{\pi w_0}, \tag{3.15}$$

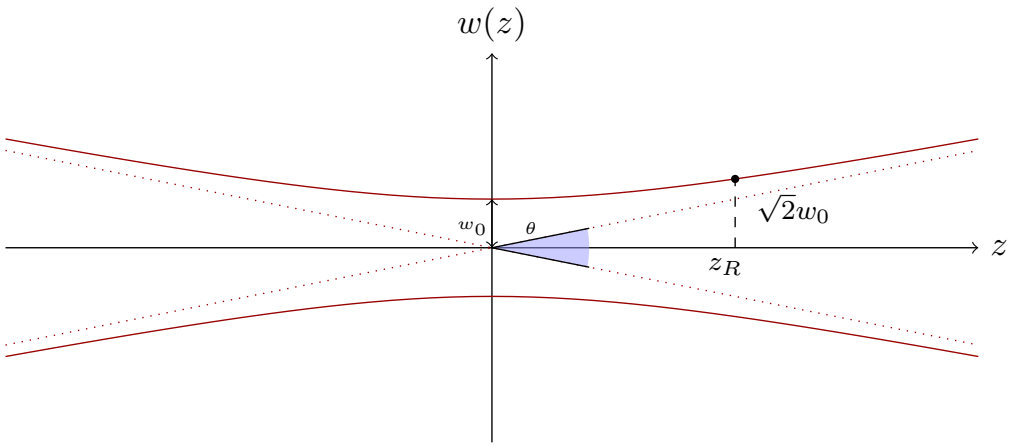

Figure 3.1: A plot of beam waist as a function of the coordinate along the cylindrical symmetry of the beam. For $z \gg z_R$ the beam waist approaches the dotted lines.

where d is the lens diameter.

3.2 Matching the radius of curvature

Formation of a standing wave between the collimator and the hemispherical mirror is achieved when the incident light is retro-reflected. The condition for retro-reflection is matching of the wavefront and mirror curvatures. From equation (3.14) the radius of curvature of the beam is given by,

$$R(z) = z\left[1 + \left(\frac{z_R}{z}\right)^2\right]. \tag{3.16}$$

The radius of curvature of the mirror is a constant R_m. It then follows that the curvature of the mirror and the beam match at,

$$z_m = \frac{1}{2}R_m + \frac{R_m}{2}\sqrt{1 - \frac{4z_R^2}{R_m}}, \tag{3.17}$$

and for $R_m \gg z_R$,

$$z_m \approx R_m - \frac{z_R^2}{R_m}, \tag{3.18}$$

which shows that for smaller z_R the beam focus (at $z = 0$) is closer to the geometric focus of the mirror.

3.3 Trapping a Particle Using Optical Forces

At the core of the optical trapping principle of the experiment lies the interplay of the *scattering force* and the *dipole force*. These forces can be seen to arise in a simplistic approach modelling

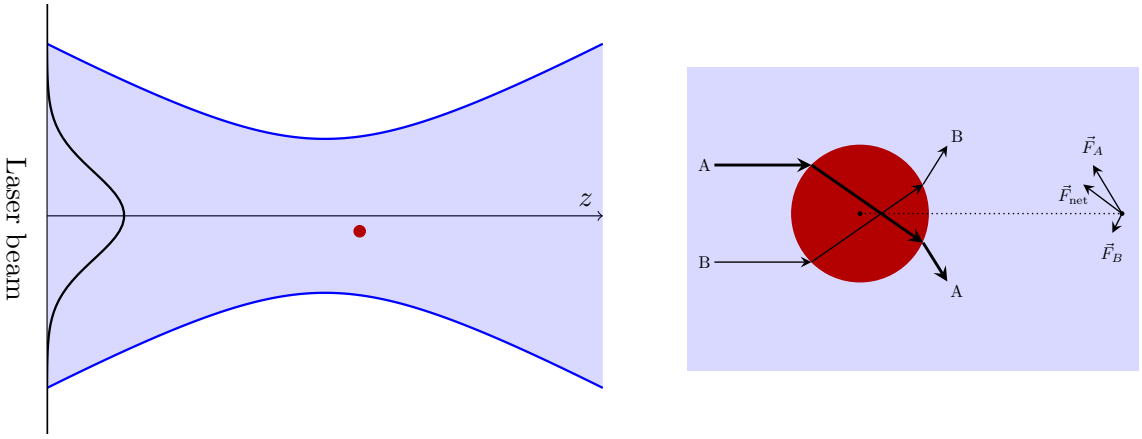

Figure 3.2: (Left) a particle trapped in a focused laser beam. The black line along the left vertical axis shows the intensity profile. (Right) the enlargement of the trapped particle depicting passing rays. The particle has an index of refraction that is greater than the surroundings. The thickness of the arrows indicates the intensity of the passing ray. The corresponding forces arising as a consequence of the dipole force are also shown. Since ray A is higher in intensity (due to the intensity gradient) it exerts a greater force on the particle. As a result, the particle is pulled towards the focus of the laser beam.

the atom as a harmonic oscillator with a driving term[3]. Firstly, considering a point dipole in an electric field. The electric field induces a dipole moment proportional to the electric field $\epsilon_0\chi_a\vec{E}$, where $\epsilon_0\chi_a$ is the dipole polarisability. The associated interaction energy is given by,

$$U = -\frac{1}{2}\epsilon_0\chi_a E^2, \tag{3.19}$$

and therefore a force,

$$\vec{F} = -\nabla U = \frac{1}{2}\epsilon_0\chi_a\nabla(E^2) = \epsilon_0\chi_a E\nabla E. \tag{3.20}$$

For a plane wave radiation linearly polarised in x direction and moving in z direction $\vec{E} = E_0\cos(\omega t - kz)\hat{\mathbf{e}}_x$ gives a z component of the force,

$$F_z = -ex\left[\frac{\partial E_0}{\partial z}\cos(\omega t - kz) + kE_0\sin(\omega t - kz)\right]. \tag{3.21}$$

In a classical model of the atom, with the electron undergoing harmonic motion with a driving term, the motion in x direction is described by,

$$\ddot{x} + \beta\dot{x} + \omega_0 x = \frac{F(t)}{m}\cos(\omega t). \tag{3.22}$$

The solution to (3.22) is given by,

$$x = u\cos(\omega t - kz) - v\sin(\omega t - kz) \tag{3.23}$$

[3] This model captures the main form of the force but doesn't reproduce the correct scaling factors, such as intensity saturation [26].

where,

$$u = \frac{\omega - \omega_0}{(\omega - \omega_0)^2 + (\frac{\beta}{2})^2}, \qquad v = \frac{-\beta/2}{(\omega - \omega_0)^2 + (\frac{\beta}{2})^2}. \tag{3.24}$$

Substituting equation (3.24) into (3.21) with the driving force $F = -eE_0$ and time averaging thus yields,

$$\langle F_z \rangle = -e \left[u \frac{\partial E_0}{\partial z} - kzE_0 \right]. \tag{3.25}$$

Result in (3.25) can be generalised to [27],

$$\langle \vec{F} \rangle = \frac{e^2}{2\epsilon_0 mc} \left[-\frac{\omega - \omega_0}{(\omega - \omega_0)^2 + (\frac{\beta}{2})^2} \frac{\nabla I}{\omega} + \frac{\beta/2}{(\omega - \omega_0)^2 + (\frac{\beta}{2})^2} \frac{I}{c} \hat{\mathbf{k}} \right], \tag{3.26}$$

for intensity of light $I = \frac{1}{2}\epsilon_0 c E_0^2$. Two distinct terms arise in (3.26). Namely, the dipole (or gradient) force proportional to ∇I and the scattering force proportional to I and pointing in the direction of wave propagation $\hat{\mathbf{k}}$. The scattering force always acts in the direction of beam propagation and arises as a consequence of momentum transfer to the particle. On the other hand, the dipole force acts towards the gradient of higher intensity when the index of refraction of the surrounding is lower than that of the trapped particle (See figure (3.2)). The particle can be stably trapped if the beams is sufficiently tight or in other words, it has a steep enough gradient to overcome the scattering force. The derivation shown does not capture all the detail and only concerns a point-like dipole rather than bulk matter, but it demonstrates that the forces that are usually presented as distinct, arise from the same phenomenon. A more rigorous treatment in the regime of interest[4] gives [28, 29],

$$\vec{F}_{\text{scatt}} = \frac{I\sigma n_m}{c} \hat{\mathbf{k}} \qquad \vec{F}_{\text{grad}} = \frac{2\pi\alpha}{cn_m^2} \nabla I \tag{3.27}$$

where n_m is the refractive index of the surrounding medium, σ is the cross section of the particle,

$$\sigma = \frac{128\pi^5 a^6}{3\lambda^4} \left[\frac{m^2 - 1}{m^2 + 2} \right]^2, \tag{3.28}$$

a is the particle radius, and α is the particle's polarisability,

$$\alpha = n_m^2 a^3 \left[\frac{m^2 - 1}{m^2 + 2} \right]. \tag{3.29}$$

In equations (3.28) and (3.29), m is the ratio of refractive indices of the particle and the surrounding medium n_p/n_m. Figure (3.3) shows the component of the forces in the z direction varied with axial distance z. The graph shows an important feature of an optical trap - in the

[4] The Rayleigh regime, when the dipole approximation applies

region around the beam focus the gradient of the force is linear and negative. Therefore, when the particle is located close to the beam focus, it experiences a linear restoring force and behaves harmonically. The gradient of the line which fits this regime is called the *trap stiffness* and classifies how strongly bound the particle is to the trap [26].

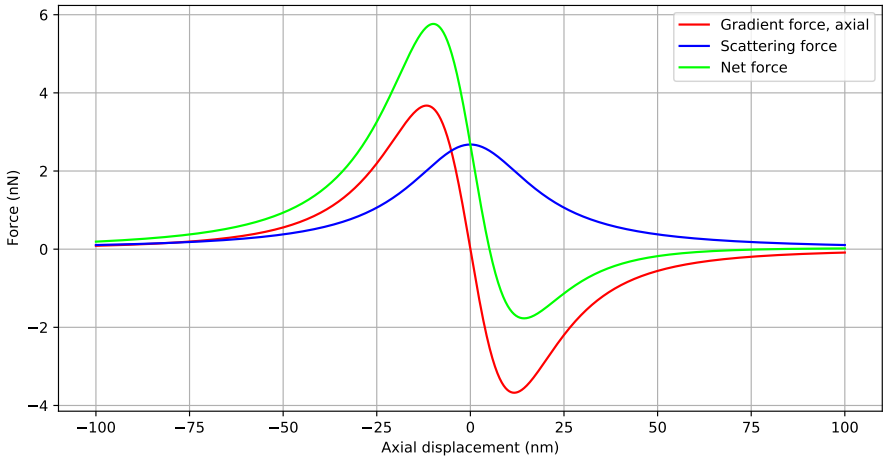

Figure 3.3: Scattering force and gradient force plotted against distance from the focus along the beam axis ($x = y = 0$) for a particle of silica ($n_p = 1.44$) with radius $a = 90$nm trapped in a Gaussian beam with waist $w_0 = 0.1\mu$m and maximum power of 1W.

3.4 Particle Dynamics

During trapping, the particle usually resides in the region of linear restoring force as showed in figure (3.3), which gives rise to the harmonic motion. A particle moving through an environment at finite pressure is subjected to a damping force, inversely proportional to the particle's velocity. When close to the focus of the laser beam, the particle is then described as a damped harmonic oscillator with a driving term,

$$\ddot{x}(t) + \Gamma\dot{x}(t) + \Omega_x^2 x(t) = \frac{F(t)}{m}, \tag{3.30}$$

and similarly for the other two directions. m is the particle mass and $F(t)$ is a stochastic force providing random kicks to the particle as a result of collisions with molecules in its environment. The force has the characteristic properties associated with Brownian motion, [30]

$$\begin{aligned} \langle F(t)\rangle &= 0, \\ \langle F(t)F(t')\rangle &= 2m\Gamma k_B T\delta(t-t'). \end{aligned} \tag{3.31}$$

By definition, the random force acts as *white noise* on the oscillatory particle, as the spectral distribution of $F(t)$,[5]

$$\begin{aligned} S_F(\omega) = \langle |F(\omega)|^2 \rangle &= \int_{-\infty}^{\infty} \langle F(t)F(t-\tau)\rangle e^{-i\omega\tau} \mathrm{d}\tau \\ &= 2m\Gamma k_B T \int_{-\infty}^{\infty} \delta(\tau) e^{-i\omega\tau} \mathrm{d}\tau \\ &= 2m\Gamma k_B T, \end{aligned} \tag{3.32}$$

is constant, where in the first line of (3.32) the Weiner-Khinchin theorem is used. Samples of white noise at different times are uncorrelated. The root-mean-square acceleration provided by the random force is the given by,

$$a_{\mathrm{RMS}} = \sqrt{\frac{\langle |F(\omega)|^2 \rangle}{m^2}} = \sqrt{\frac{2\Gamma k_B T}{m}}, \tag{3.33}$$

which was used when simulating particle dynamics as the spread of the Weiner process in the Euler-Mayurama method (see Appendix section 8.1).

3.5 Power Spectral Density

Power spectral density, usually abbreviated PSD, is a useful tool in extracting information from a time sequence as it allows to see the power content[6] in any frequency interval. It is a different way of expressing the same information about the time sequence but usually is more accessible. PSD of the particle's position allows to deduce many useful quantities - trap frequency, damping rate, average square position, center of mass temperature to name a few [15]. It is defined as,

$$S_{xx}(\omega) = |\hat{x}(\omega)|^2, \tag{3.34}$$

where $\hat{x}(\omega)$ is the Fourier transform of $x(t)$,

$$\hat{x}(w) = \int_{-\infty}^{\infty} e^{-i\omega t} x(t) \mathrm{d}t. \tag{3.35}$$

To find S_{xx}, a Fourier transform is applied to equation (3.30) to obtain,

$$(-\omega^2 - i\omega + \Omega_x^2)x(\omega) = \frac{F(\omega)}{m}, \tag{3.36}$$

[5] Weiner-Khinchin theorem relates the autocorrelation of a random stationary process ($\langle F(t)\rangle = q$ where q is constant in time) to the corresponding power spectrum.

[6] The term 'power' or 'energy' in this context represents a general notion of power or energy to express the idea of which parts of the signal contribute most to its variation

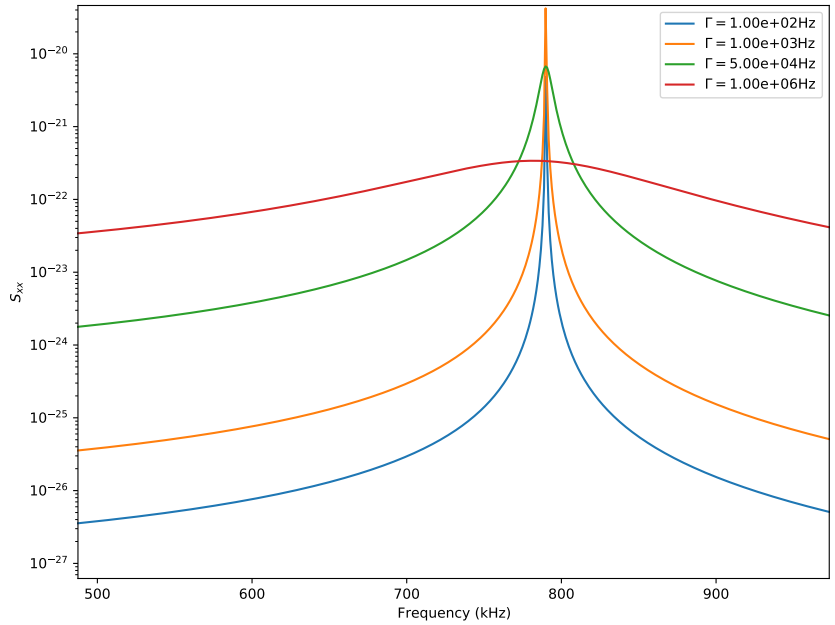

Figure 3.4: Power spectral density of the position x for different values of the damping rate Γ for a particle of mass $m = 10^{-18}$kg, temperature $T = 300$K, and trap frequency in x $\Omega_x = 2\pi \times 790$kHz. Here the units of S_{xx} are arbitrary, but usually the PSD is expressed in units of W/Hz

then averaging and rearranging,

$$S_{xx}(\omega) = \langle |x(w)|^2 \rangle = \frac{\langle |F(\omega)|^2 \rangle}{m^2 \left[(\Omega_x^2 - \omega^2)^2 + \Gamma^2 \omega^2 \right]}. \tag{3.37}$$

Quantity $\langle |F(\omega)|^2 \rangle = S_F(\omega)$ which was calculated in the previous section. Finally,

$$S_{xx}(\omega) = \frac{2k_B T \Gamma}{m \left[(\Omega_x^2 - \omega^2)^2 + \Gamma^2 \omega^2 \right]}. \tag{3.38}$$

Figure (3.4) shows S_{xx} graphically for different values of the damping rate Γ. It shows that the smaller the value of Γ, the more defined features of the PSD. The resonant spike is centred on the trap frequency Ω_x with the width defined by Γ. Therefore, the width of S_{xx} is indicative of the local pressure in the vicinity of the particle. To demonstrate its usage further, one useful examples is using the PSD to obtain the average square position. $\langle x^2 \rangle$ can be found by summing over positive frequency contributions and averaging, and therefore,

$$\langle x^2 \rangle = \int_0^\infty S_{xx}(\omega) \mathrm{d}\omega. \tag{3.39}$$

Many other quantities can be obtained such as the centre of mass temperature through considerations of equipartition theorem. However, S_{xx} was not directly observed in the experiment of this project. Instead the PSD corresponding to the interferometric signal was observed. The signal's spectral density has a much more complicated structure [31] but encompasses the same information.

3.6 Kalman Filter

The experiment does not provide a direct readout of particle position within the trap. Rather, the information about particle position is hidden within a noisy interferometric signal. In a situation where the desired information about a state of a system is not directly accessible and instead only an indirect measurement infested by noise is available, the Kalman filter is a powerful tool to make an optimal estimate of the state. The *state* of the system can be any set of desired properties of the observed system in question, given that two conditions are met. Namely, that is we have some model which allows us to estimate how the system will evolve in time. In the particular case studied in this project, the state of interest is the position and the velocity of the particle. We also require to have means to take measurements which provide information about the quantity of interest, whether directly or indirectly[7]. In the standard Kalman filter the relationship between the true value of the state[8] x and the measured quantity is required to be linear,

$$\mathrm{z}_k = \mathbf{H}x_k + \mathrm{v}_k, \tag{3.40}$$

where H is the matrix which maps the true state vector of the system x_k at time k to the corresponding measurement z_k, and v_k is Gaussian distributed white noise. Similarly for the system dynamics, the prediction of the future state is required to be linear, encompassed by the state extrapolation equation,

$$\mathrm{x}_{k+1} = \mathbf{F}\hat{\mathrm{x}}_k + \mathbf{G}\mathrm{u}_k + \mathrm{w}_k. \tag{3.41}$$

The hat above the state vector indicates that it is a so-called *a posteriori* state; The state corrected by accounting of the most recent observations of the system. On the other hand, the state without the hat indicates that it is an *a priori* state; a predicted state using only the knowledge of system dynamics. Matrices $\mathbf{F}$ and $\mathbf{G}$ are the *transition matrix* and the *control matrix* respectively. They map the a posteriori state from time step k to a priori state of time step $k+1$. The only difference between $\mathbf{F}$ and $\mathbf{G}$ is that the transition matrix encompasses the dynamics which depend on the previous state of the system, whilst the control matrix encompasses the dynamics independent of the state. Vector w_k is called the *process noise*. It encompasses the dynamics that affect the evolution of the state, but cannot be accounted due to their random nature. Similarly to the measurement noise v_k, the process noise is assumed to be Gaussian distributed white noise.

Figure 3.5 shows diagrammatically each step of the Kalman filter's operation. The process is

[7] In cases when the state components are related by system dynamics, a measurement of only one of them is sufficient to accurately estimate the both. This is the case for the position and velocity.

[8] **Notation:** the true value of the state is denoted by italicised 'x' whilst estimates are denoted by 'x'

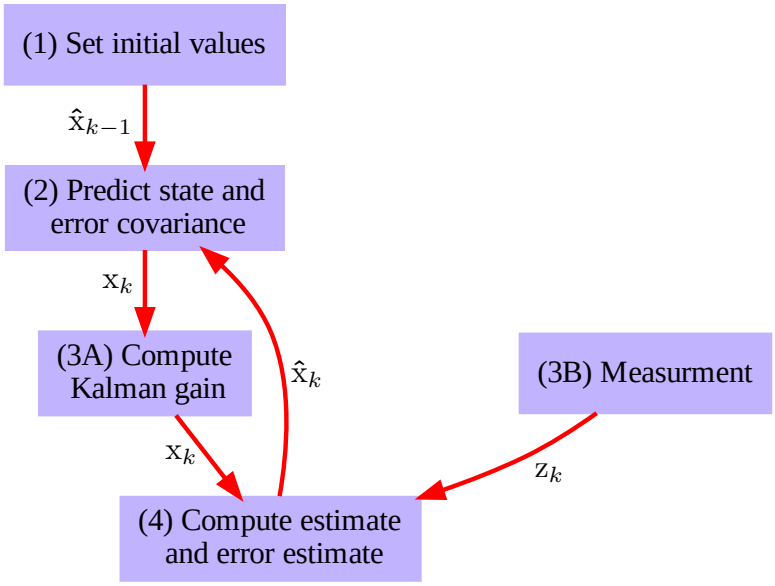

Figure 3.5: A diagram showing the operation of the Kalman filter. Arrow labels indicate the evolution of the state at different steps in the algorithm.

as follows:

1. **Set initial values.** To begin using the Kalman filter an initial guess of the state components and the associated covariance matrix are needed for the first iteration. The state is a vector and the covariance matrix contains the variances associated to the state and the cross correlations. For example in 2 dimensions the state vector and the covariance matrix are of the form,

$$\hat{x}_0 = \begin{bmatrix} a \\ b \end{bmatrix} \quad \text{and} \quad \hat{\mathbf{P}}_0 = \begin{bmatrix} \sigma_{aa}^2 & \sigma_{ab}^2 \\ \sigma_{ba}^2 & \sigma_{bb}^2 \end{bmatrix}. \tag{3.42}$$

   where a and b are quantities of interest such as the position and velocity. The initial states are denoted with hats, indicating that they are a posteriori states. This is because at this point in the algorithm, the initial state and the covariance matrix are estimates which represent our best knowledge of the state.

2. **Predict state and error covariance.** As explained above, equation (3.41) is used to extrapolate the a posteriori state estimate $\hat{x}_0$ to an a priori state estimate x_1 for the next time step. How system dynamics can be translated to those of the form given in equation (3.41) is demonstrated in section 6.2. Similarly to the state vector, the covariance matrix also has to be progressed in time to accurately describe the updated state vector x_1. It can be derived [32] from the state update equation that the evolution of the covariance matrix in time is described by,

$$\mathbf{P}_{k+1} = \mathbf{F}\hat{\mathbf{P}}_k\mathbf{F}^{\mathrm{T}} + \mathbf{Q}, \tag{3.43}$$

   where $\mathbf{Q} = \mathrm{E}[w_k^{\mathrm{T}} w_k]$ is the covariance matrix associated to the process noise. Addition of

$\mathbf{Q}$ to the future a priori state $\mathbf{P}_{k+1}$ expresses the fact that every time step adds uncertainty to the knowledge of the state due to unaccountable random dynamics in the form of process noise. Therefore, at this step of the Kalman filter, the state estimate and the covariance matrix are transformed such that $(\hat{\mathrm{x}}_0, \hat{\mathbf{P}}_0) \mapsto (\mathrm{x}_1, \mathbf{P}_1)$.

3. (A) **Compute Kalman gain.** The *Kalman gain* is a quantity which arises when we seek minimisation of the covariance matrix,

$$\mathbf{K}_k = \mathbf{P}_k\mathbf{H}^{\mathrm{T}}(\underbrace{\mathbf{H}\mathbf{P}_k\mathbf{H}^{\mathrm{T}}}_{\substack{\text{covariance of}\\ \text{the expected}\\ \text{measurement}}} + \underbrace{\mathbf{R}}_{\substack{\text{covariance of}\\ \text{the observed}\\ \text{measurement}}})^{-1}, \tag{3.44}$$

where $\mathbf{R} = \mathrm{E}[\mathrm{v}_k^{\mathrm{T}}\mathrm{v}_k]$ is the measurement covariance. Akin to the process noise in equation (3.43), it adds uncertainty at every update of the Kalman gain to account for inevitable measurement noise, always present when a measurement is taken. The Kalman gain quantifies how much we trust the measurement z_k relative to the predicted estimate of the measurement $\mathbf{H}\mathrm{x}_k$. As in equation (3.40), $\mathbf{H}$ encodes the measurement model and tells us the expected outcome of the measurement. (B) **Perform a measurement** z_k ready for the final step of the Kalman filter.

4. **Compute state estimate and error estimate.** The purpose of this step is to update the state estimate with the available information - the observation z_k with the associated Kalman gain $\mathbf{K}_k$. An update to the a priori state estimate x_k is computed using, [32]

$$\hat{\mathrm{x}}_k = \mathrm{x}_k + \mathbf{K}_k(z_k - \mathbf{H}\mathrm{x}_k), \tag{3.45}$$

and,

$$\hat{\mathbf{P}}_k = (\mathbf{I} - \mathbf{K}_k\mathbf{H})\mathbf{P}_k, \tag{3.46}$$

where $\mathbf{I}$ is the identity matrix. The state update equation is found by finding the Gaussian distribution which gives probability of the expected measurement given the observed measurement. More specifically, having access to the prior probability distribution for the expected measurement $P[\mathbf{H}\mathrm{x}_k]$ the aim is to find the posterior probability distribution $P[x_k|z_k]$ which accounts for the knowledge of the observation made of x_k. Using Bayes' theorem,

$$P[\mathbf{H}\mathrm{x}_k|\mathrm{z}_k] = \frac{P[\mathrm{z}_k|\mathbf{H}\mathrm{x}_k]P[\mathbf{H}\mathrm{x}_k]}{P[\mathrm{z}_k]} \tag{3.47}$$

where we can ignore $P[\mathrm{z}_k]$ and normalise the posterior distribution later. As mentioned above, we have access to the prior probability distribution modelled by a Gaussian distribution $P[\mathbf{H}\mathrm{x}_k] = N[\mathbf{H}\mathrm{x}_k, \mathbf{H}\mathbf{P}_k\mathbf{H}^{\mathrm{T}}]$[9]. Similarly, $P[\mathrm{z}_k|x_k]$ is obtained from the measurement

[9] **Notation:** $N[\cdot]$ denotes the normal distribution

model, in equation (3.40). In the Kalman filter, it is assumed that the state is Gaussian distributed and the linearity of the measurement model preserves the Gaussian nature. Therefore, $P[\mathrm{z}_k|\mathbf{H}\mathrm{x}_k] = N[\mathrm{z}_k, \mathbf{R}]$. A product of two Gaussian PDFs is also Gaussian. The resulting Gaussian posterior has mean and covariance given by, [32]

$$\begin{aligned} \mathbf{H}\hat{\mathrm{x}}_k &= \mathbf{H}\mathrm{x}_k + \mathbf{H}\mathbf{P}_k\mathbf{H}^{\mathrm{T}}(\mathbf{H}\mathbf{P}_k\mathbf{H}^{\mathrm{T}} + \mathbf{R})^{-1}(\mathrm{z}_k - \mathbf{H}\mathrm{x}_k) \\ \mathbf{H}\hat{\mathbf{P}}_k\mathbf{H}^{\mathrm{T}} &= \mathbf{H}\mathbf{P}_k\mathbf{H}^{\mathrm{T}} - \mathbf{H}\mathbf{P}_k\mathbf{H}^{\mathrm{T}}(\mathbf{H}\mathbf{P}_k\mathbf{H}^{\mathrm{T}} + \mathbf{R})^{-1}\mathbf{H}\mathbf{P}_k\mathbf{H}^{\mathrm{T}} \end{aligned} \tag{3.48}$$

which reduce to equations (3.45) and (3.46) upon cancellation of redundant $\mathbf{H}$ and $\mathbf{H}^{\mathrm{T}}$ matrices. In equation (3.45) the Kalman gain is acts as a weight for the *measurement residual* $\mathrm{y}_k = \mathrm{z}_k - \mathbf{H}\mathrm{x}_k$. The update state and can be intuitively thought of as a measure of trust in the measurement. The updated state represents the best state of knowledge for the state estimate for this time step. The a posteriori estimate is then used for the extrapolation to the next time step, and the algorithm repeats recursively from step (2).

This completes the description of the linear Kalman filter. The algorithm acts as an optimal estimator for systems which can be described by linear system dynamics and measurement. Although system dynamics of the particle in the trap are linear, the relationship of the position to the measured quantity is not. A modified version of the Kalman filter is needed to address the nonlinearities, which is the subject of the next section.

3.7 Unscented Kalman Filter

While it is fair to assume that the components of the state are Gaussian distributed, nonlinear relationships of the state to the dynamics or the measurement, lead to a vastly different probability density function. This is demonstrated in figure (3.6). The interferometric signal measured during trapping has the form,

$$V = V_0 \sin(\kappa z(t) + \theta(t)) \tag{3.49}$$

where V_0, κ, ϕ are the signal amplitude, rate of change of phase with position and a slowly drifting random phase respectively. This form of measurement is highly nonlinear. The standard Kalman filter described in the previous section heavily relies on the state estimate distribution retaining its Gaussian form at every step of the algorithm, hence it is not applicable in this case.

There are many modifications of the Kalman filter designed to expand onto nonlinear problems. One of the early and successful modifications is the *extended Kalman filter*. It does not modify the algorithm itself but rather the problem in question; the system dynamics and measurement are linearlised through a clever change of variables, such that the Kalman filter is applicable. This method relies on the Taylor approximation and is therefore only capable of capturing the

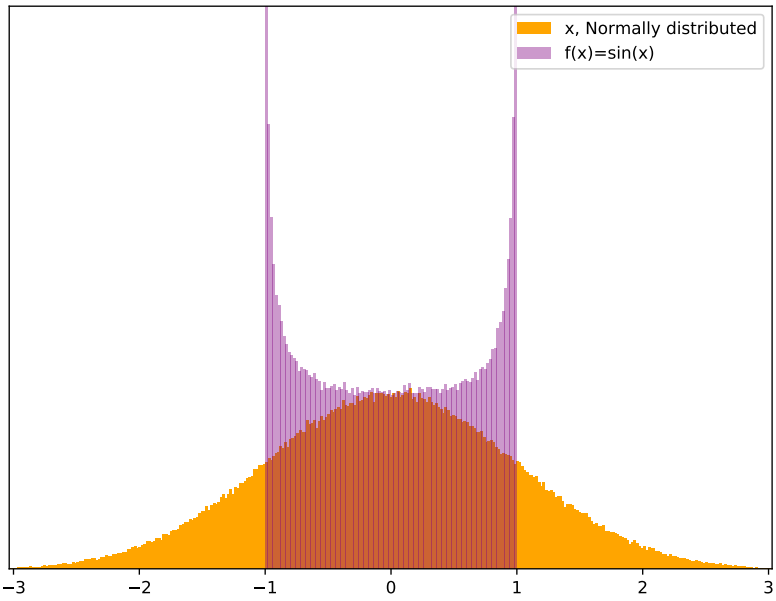

Figure 3.6: The orange histogram shows a sample of 500000 normally distributed points x. The purple histogram shows the distribution of the same sample when the nonlinear function $f(x) = \sin(x)$ is applied to each point. Both histograms are area normalised.

first order accuracy [33]. When applied to highly nonlinear systems, the filter has a tendency to diverge [32]. It also requires the calculation of derivatives at every time step which can be computationally expensive.

Another alternative is the *Monte Carlo Kalman filter*[10]. This is a highly preferable alternative, as the this filter is not constrained to weak nonlinearities. This is because it relies on reconstructing the probability density function distorted by nonlinearities through sampling. At each time step, the filter generates a large number of points selected at random and passes them through the nonlinear function. This process allows to build up the distorted distribution, as it was done in figure (3.6). From the output, the mean and variance can then be calculated to approximate a Gaussian then use the Kalman filter as usual. This approach is highly effective, being able to resolve even highly nonlinear functions given that enough points are sampled. However, the large number of randomly selected points, called *sigma points*, give rise to the largest disadvantage for the particular case of considered in this project. As the final goal of developing the protocol of site hopping is to be able to perform this signal analysis in real-time during trapping, the filter needs to operate extremely quickly. Generation of thousands of sigma points at every time step therefore forms a major obstacle.

[10] This is a general type of Kalman filters using random numbers to sample the prior and posterior probability distribution. Examples of such filters are the ensemble and the particle Kalman filter.

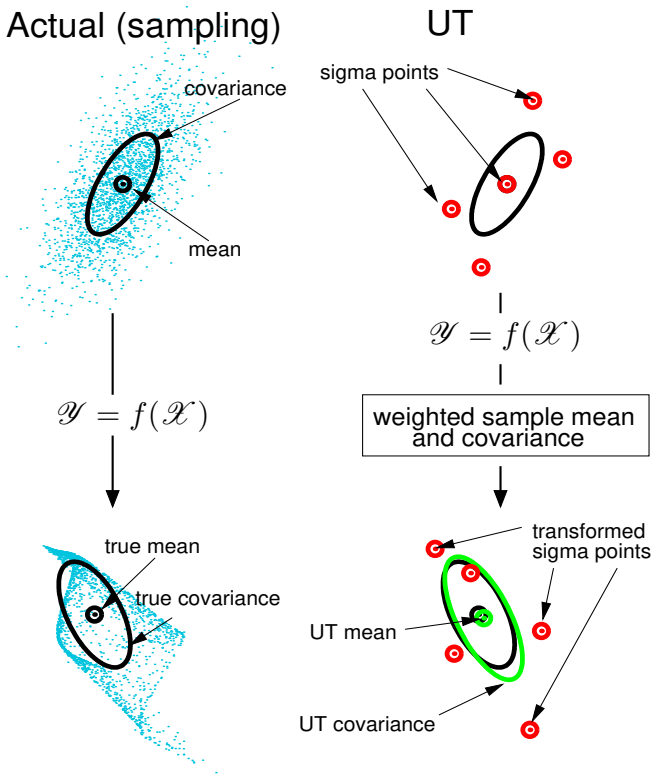

Figure 3.7: A diagram showing the difference between the unscented and Monte Carlo type filters. (Left) many sigma points are chosen at random. The large number of points allows to reconstruct the distorted distribution and approximate a Gaussian which represents it. All points are equally weighted. (Right) The few sigma points are passed through the Unscented Transform (UT). Adapted from [33].

The Unscented Kalman filter (UKF) was chosen as the main tool for inferring the state of the particle. Similarly to a Monte Carlo based approach described above, the filter relies on sampling the nonlinear distribution. However, in this case the filter relies on a deterministic sampling scheme of sigma points [34]. The Unscented Kalman filter can be sufficiently accurate, but in most cases only requires only a few sigma points per dimension of the problem [35], making it highly robust. This is depicted in figure (3.7). Similar accuracy to Monte Carlo type filters is achieved due to a clever weighting of the few sigma points that are selected. For the remainder of this section an outline of the changes to the Kalman filter that implements the Unscented Kalman filter.

In the Unscented Kalman filter, the state extrapolation, state update and the Kalman gain are computed differently. Starting from the prediction step, a set of N sigma points $\mathcal{X}_i = [\mathcal{X}_0, \mathcal{X}_1, .., \mathcal{X}_L]_i^{\mathrm{T}}$ are selected, where L is the dimension of the state vector and $i = 0, .., N$.

In addition, 2 weights W_i^{m} and W_i^{c} are selected for each sigma point, which need to satisfy,

$$\begin{aligned} \sum_{j=0}^{N} W_j^m &= 1, \\ \sum_{j=0}^{N} W_j^c &= 1. \end{aligned} \tag{3.50}$$

The weights are used to compute the mean and covariance of the transformed sigma points, which is discussed below. There is no strict rule for selecting the sigma points and the weights. Rather, the user is free to select the number and position of the points that will suit the problem. Commonly, the choice is simplified with the use of functions which choose the numbers, positions and corresponding weights of the points, controlled by user set parameters. For the purpose of this study, the sigma points and their weights were selected using the popular parametrisation first introduced by Eric A. Wan and Rudolph van der Merwe [33],

$$\begin{aligned} (\mathscr{X}_0)_k &= \hat{\mathrm{x}}_k, \\ (\mathscr{X}_i)_k &= \hat{\mathrm{x}}_k + \left(\sqrt{(L+\lambda)\hat{\mathbf{P}}_k}\right)_i, \quad i = 1, ..., L \\ (\mathscr{X}_i)_k &= \hat{\mathrm{x}}_k - \left(\sqrt{(L+\lambda)\hat{\mathbf{P}}_k}\right)_{i-L}, \quad i = L+1, ..., 2L \\ W_0^m &= \frac{L}{L+\lambda}, \\ W_0^c &= \frac{L}{L+\lambda} + (1 - \alpha^2 + \beta), \\ W_i^m &= W_i^c = \frac{L}{2(L+\lambda)} \quad i = 1, ..., 2L \end{aligned} \tag{3.51}$$

where L is the dimension of the state vector, α is a user parameter which determines the spread of the sigma points, $\lambda = \alpha^2(L + \kappa) - L$ is a scaling parameter with another secondary scaling parameter κ. β encompasses the prior knowledge of the distribution of $\hat{\mathrm{x}}_k$. $(\sqrt{(L+\lambda)\hat{\mathbf{P}}_k})_i$ is the ith row of the matrix square root.

Once the sigma points and weights are generated, the a priori estimate for the current time step is generated by first passing the sigma points through a nonlinear function $f(\cdot)$ describing the system dynamics,

$$(\mathscr{Y}_i)_k = f((\mathscr{X}_i)_{k-1}). \tag{3.52}$$

Then, the a priori state estimate and variance are generated using,

$$\begin{aligned} \mathrm{x}_k &= \sum_{i=0}^{2L} W_i^m (\mathscr{Y}_i)_k, \\ \mathbf{P}_k &= \sum_{i=0}^{2L} W_i^c ((\mathscr{Y}_i)_k - \mathrm{x}_k)((\mathscr{Y}_i)_k - \mathrm{x}_k)^{\mathrm{T}} + \mathbf{Q}. \end{aligned} \tag{3.53}$$

In UKF this step is called applying the *Unscented transform*[11]. The a posteriori estimate is generated very similarly, by first passing the transformed sigma points $(\mathscr{Y}_i)_k$ through a nonlinear function $h(\cdot)$ encompassing the measurement model,

$$(\mathscr{Z}_i)_k = h((\mathscr{Y}_i)_k). \tag{3.54}$$

A Gaussian distribution corresponding to the measurement is then approximated with the mean and covariance,

$$\begin{aligned} (\mu_z)_k &= \sum_{i=0}^{2L} W_i^m (\mathscr{Z}_i)_k, \\ (\mathbf{P}_z)_k &= \sum_{i=0}^{2L} W_i^c ((\mathscr{Z}_i)_k - \mu_z)((\mathscr{Z}_i)_k - \mu_z)^{\mathrm{T}} + \mathbf{R}. \end{aligned} \tag{3.55}$$

The posterior estimate is obtained in a similar fashion to equation (3.45),

$$\hat{\mathrm{x}}_k = \mathrm{x}_k + \mathbf{K}_k(\mathrm{z}_k - (\mu_z)_k), \tag{3.56}$$

but with the Kalman filter calculated using,

$$\mathbf{K}_k = (\mathbf{P}_{xz})_k (\mathbf{P}_{zz})_k^{-1} \tag{3.57}$$

where,

$$\begin{aligned} (\mathbf{P}_{xz})_k &= \sum_{i=0}^{2L} W_i^c ((\mathscr{Y}_i)_k - \mathrm{x}_k)((\mathscr{Z}_i)_k - \mu_z)^{\mathrm{T}}, \\ (\mathbf{P}_{zz})_k &= \sum_{i=0}^{2L} W_i^c ((\mathscr{Z}_i)_k - \mu_z)((\mathscr{Z}_i)_k - \mu_z)^{\mathrm{T}} + \mathbf{R}. \end{aligned} \tag{3.58}$$

This is analogous to how the Kalman gain was computed in the previous section, as it can be thought of as quantifying the belief in the measurement z_k relative to the prior estimate. Lastly, the posterior covariance is generated with,

$$\hat{\mathbf{P}}_k = \mathbf{P}_k - \mathbf{K}_k(\mathbf{P}_z)_k \mathbf{K}_k^{\mathrm{T}}, \tag{3.59}$$

[11] The name 'unscented' given to the algorithm bares no technical significance; It is an arbitrary name given to the algorithm by its creator Jeffrey Uhlmann.

which is the last change to the original Kalman filter, allowing now to implement the Unscented Kalman filter. Section 6 focuses on the specifics of how to apply the UKF algorithm to the problem of transferring the particle between intensity maxima, code for which was provided in the appendix section 8.3. The next section focuses on describing the apparatus used in particle trapping and explains their principle of operation.

4 Apparatus

The experiment was built mostly using a single mode optical fibre, carrying TEM_{00} mode industry standard 1550nm light. A single mode fibre consists of a thin pure silica core which contains the laser light, surrounded by protective cladding. The 1550nm laser was generated using a fibre seed laser[12] and amplified using Erbium-doped fibre amplified (EDFA). This section discusses the principle of operation and usefulness of the tap coupler and the circulator - two key fibre optic components used in the experiment. A brief description of the vacuum system is also provided. The final section 4.4 describes the principle of operation of the vibrating-mesh nebuliser which was used to load the particle into the trap site.

4.1 Tap Couplers

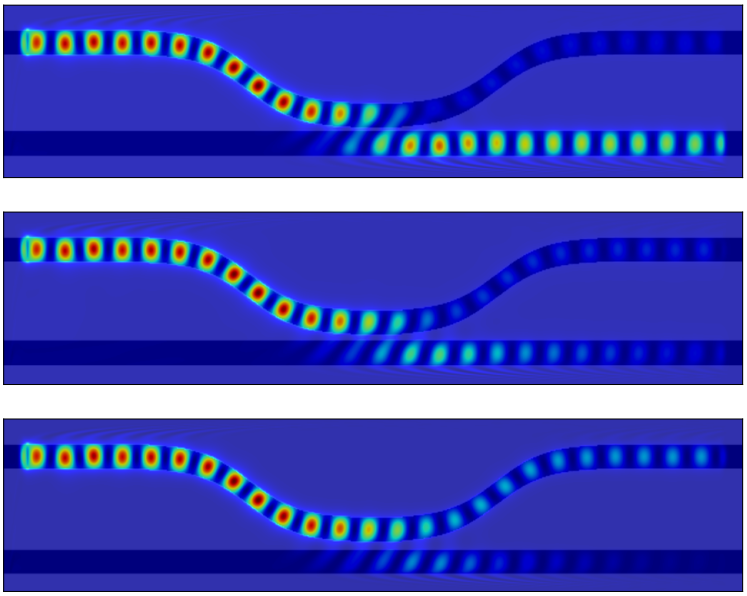

Figure 4.1: Spatial distribution of power in a 2D simulation of the power transfer in a tap coupler for three different separations of two optical fibres. A flow of energy was initiated in `IN-1` (as in figure 4.2) which leaks to ports `OUT-1` and `OUT-2` via the evanescent field.

Tap couplers are optical fibre components which were used in the experiment to passively measure and reduce the power of the passing optical signal. The principle of their operation is the exploitation of power leakage of an evanescent field from one optical fibre to another in its vicinity. The amount of power which leaks through depends on the separation of cores of the two optical fibres. This phenomenon was demonstrated in figure 4.1. It shows that the division of

[12] `LN-focus-32`

power is highly sensitive to the separation of the fibres and can be finely tuned to achieve the desired effect. When the fibres are separated by a larger distance, less evanescent field couples to the second fibre. In the experiment, optical couplers were used to monitor powers at different points in the experimental setup and to reduce the power across vulnerable components such as the photodiode. Couplers are usually referred to by their power division ratio sometimes expressed in decibels (see figure 4.2)

Coupler Losses (dB)

	OUT-1	OUT-2
IN-1	0.5	10
IN-2	10	0.5

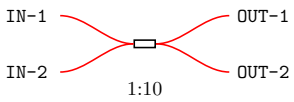

Figure 4.2: (Left) Example of losses in a tap coupler connecting different ports. (Right) Diagram of a tap coupler. The label '1:10' indicates the power division between ports `OUT-1` and `OUT-2`

4.2 Circulators

Circulators are fibre optic devices used in the experiment to rectify and direct backscattered light, ensuring that the components which cannot handle high powers do not get damaged. Light moving through a circulator has a direction-dependent output. Figure (4.3) shows the three paths that characterise the circulator used[13] in this project.

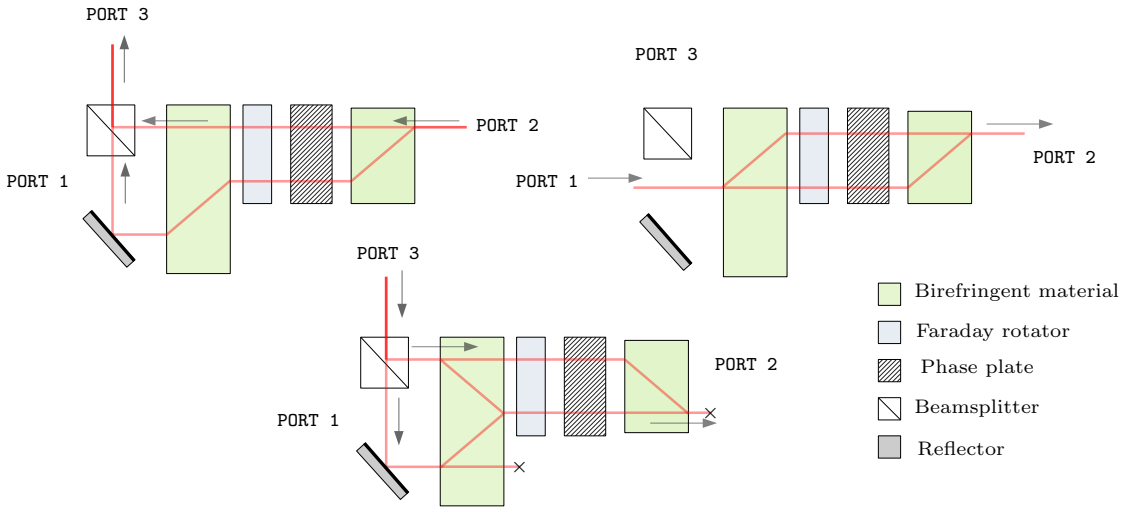

Figure 4.3: Light travel paths in a three-way circulator. Separated beams are always recombined at the output. In this design light travelling from `PORT 3` to `PORT 2` (bottom) is filtered out.

The principle of operation of the optical circulator is based on the clever arrangement of a Faraday

[13] Model no. `HCIR-3-P-1550-900-1-1-NE-5.5x50-5W`

rotator and birefringent materials to yield a direction-dependent output. The beam is split into two orthogonal polarisations and recombined at the output, as much more energy is lost if instead unwanted polarisations of light are discarded [36]. The splitting and manipulations of orthogonally polarised light is done using a beamsplitter and 45° birefringent materials respectively, as shown in figure (4.3). Due to imperfections in manufacture, the polarisation-dependent components sometimes allow the light to pass through the wrong port. This small error amounts to about a 50dB power leaks through to a wrong port.

4.3 Vacuum System

Trapping of the nanoparticle took place in a vacuum chamber, evacuated using two pumps operating in different pressure regimes - a scroll pump (`Edwards nXDS6i`) used to bring the pressure down to about 10^{-2} mbar from atmospheric pressure, and a turbo pump (`Pfeiffer HiPace 80`) to further lower the pressure to about 10^{-11} mbar.

Pressure was controlled using two valves, as shown in figure (4.4). Mainly, the pressure was controlled using the fine pressure control valve ((R1) in the figure) installed to be used with the flange gate connecting the trap site and the pumps closed. The coarse pressure control valve can be used to lower the pressure in the chamber ((R5) in the figure) but it usually resulted in the particle being lost due to turbulent flow. Although slow, controlling the pressure using the pressure valve led to the fewest losses of the particle during trapping, allowing to initiate the turbo pump when low enough pressure was reached.

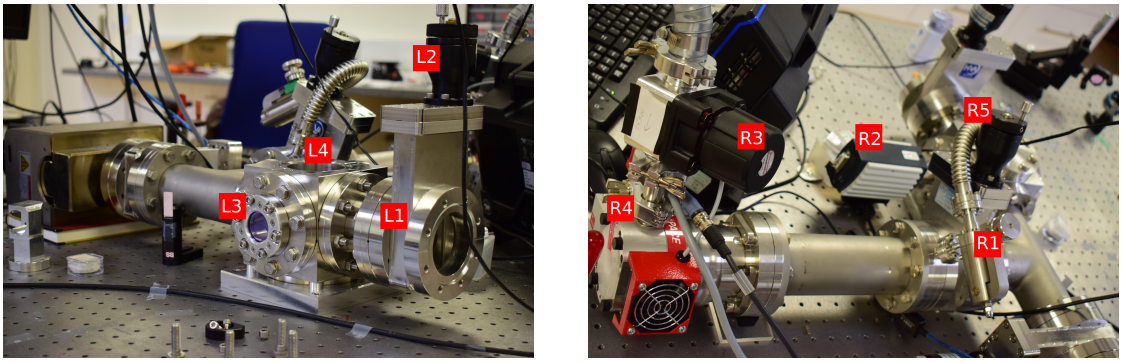

Figure 4.4: A front and back view picture showing the vacuum chamber used for trapping (Left) Front view (L1) Flange opening used to introduce the nanoparticles into the trap (L2) Valve used to seal the flange gate (L3) Viewport onto the hemispherical mirror/lens (L4) Flange opening through which the lens was mounted (Right) Back view (R1) Fine pressure control valve (R2) Pressure gauge (R3) Scroll pump valve (R4) Turbo pump (R5) Coarse pressure control gate valve

Live pressure measurements were obtained using a (`Leybold ITR 90`) gauge. This is a hot cathode ionisation gauge - an electron current emitted from a heated filament collides with gas molecules

from the chamber. The current of ionised molecules is then measured which translates to a pressure reading. Pressure readings produced above around 300 mbar were highly fluctuating and unreliable, but still served as a rough guide in controlling the pressure valves.

4.4 Nebuliser

Loading of the particle into the trap site was achieved using a medical nebuliser. This approach has proven to be very effective relative to alternative approaches involving the particle being attached to a substrate. In those approaches precise control of nanoscopic forces is required to overcome Van der Waals attraction. The small size of the trapping region introduces many technical difficulties to the process of removing the particle from the surface. On the other hand, the nebuliser produces an aerosol of slow-moving nanoparticles, able to be captured in the laser focus. Even if loaded from a large distance, the high spread of nanoparticles can be contained using a shield, as was done in the experiment (See section 5.5). This ensured that the aerosol dispersed only in a small region around the focus of the beam.

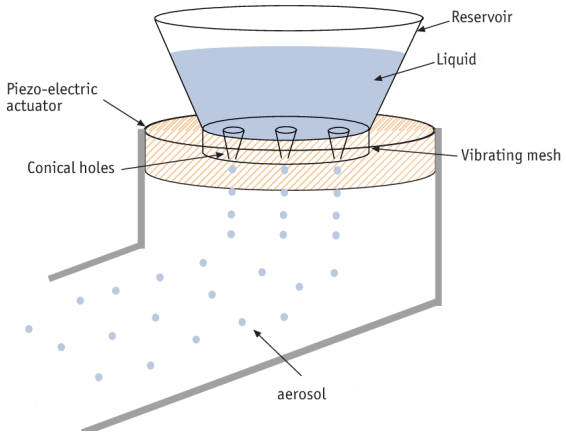

Figure 4.5: Diagram showing operation of the nebuliser. Adapted from [37].

The principle of operation is depicted in figure (4.5). A liquid solution containing nanoparticles is brought in contact with the mesh. The piezoelectric element causes the mesh to vibrate, forcing single droplets of the liquid through the laser-drilled conical holes. A solution is prepared such that each droplet contains one or no nanoparticles on average.

5 Experimental Work

Experimental work in the project began with building a setup for the purpose of alignment of the laser beam with different optics. Figure 5.1 (Left) shows the first and very brief stage of the experiment used to align the laser beam with a flat mirror. This setup was used as a learning tool for the experimental techniques as well as to identify any hidden power losses. Progressing towards trapping with hemispherical mirror, figure 5.1 (Right) shows the next stage of the experiment in which the collimator was instead aligned with a hemispherical mirror, mounted in the vacuum chamber. A plano-convex lens was later introduced. Alignment at this stage is described in more detail in section 5.1.

The ultimate goal of the project was to trap a nanoparticle in vacuum with position readout, then explore the possibility of Rayleigh scatter suppression. This final stage and trapping with the hemispherical mirror was never reached. Although Rayleigh scatter suppression was not considered, nanoparticles were successfully trapped as described in section 5.5. All the work done involving the mirror is also documented in the following sections.

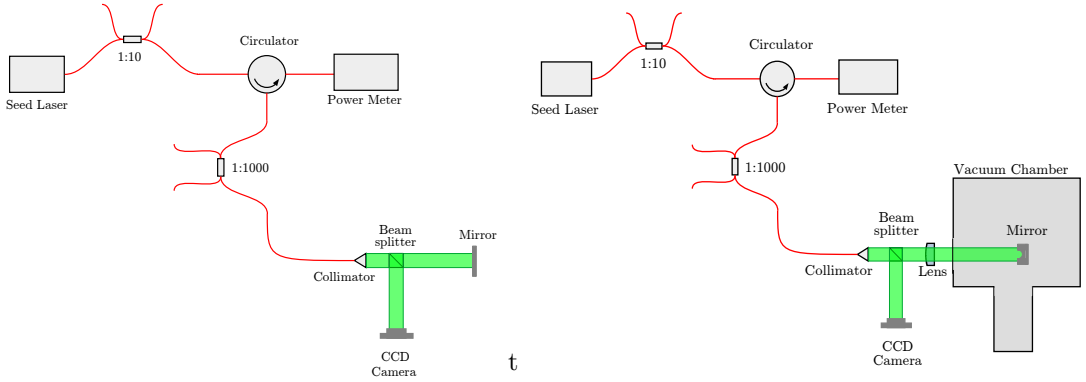

Figure 5.1: Alignment stage of the experimental setup. The 1550nm laser was directed to the collimator. Back-reflected light was directed to the power meter. Live CCD camera image observation was used to aid alignment. **Left** Alignment with the flat mirror **Right** Alignment with the hemispherical mirror and a plano-convex lens. The vacuum chamber at this stage was not evacuated.

5.1 Lens and Hemispherical Mirror Alignment

In preparation for the final stage of the experiment the first objective was to align the hemispherical mirror with the output beam from the collimator and measure the back-reflected light coupled back into the collimator. The mirror was mounted inside the vacuum chamber from the previous experiment conducted at the lab. Alignment was done by adjusting the position of the collimator

which was placed in a 3-axis translation mount and with aid of a fluorescent beam card. A pellicle beam splitter was placed between the collimator and the mirror to direct a fraction of the light towards a CCD camera. Position changes were based on the CCD camera image which, upon good alignment, showed the Arago spot and rings produced by diverging laser light (see figure 5.2). The distinct pattern arises as a consequence of Fresnel diffraction, when light shines on a circular obstacle. The diverging laser light produced the brighter area around the rim of the hemispherical mirror. After successful alignment, a plano-convex lens was introduced between the collimator and the window of the vacuum chamber. Alignment was repeated for the lens, also placed on a 3-axis translation stage.

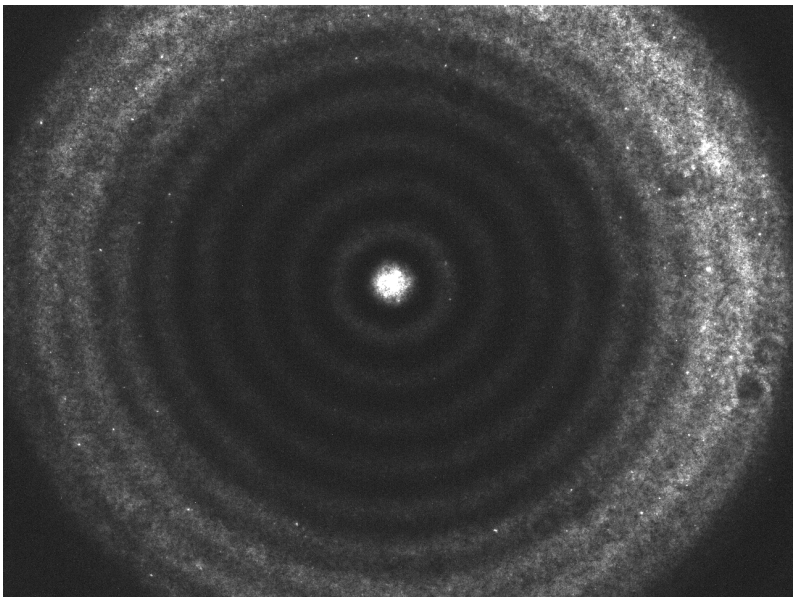

Figure 5.2: The Arago spot with rings produced by the diverging light captured using the CCD camera upon alignment of the laser beam with the hemispherical mirror (as in figure 5.1 (Right) but without the lens in place). The laser beam overfills the circular aperture corresponding to the hemispherical mirror, indicated by the brighter area around the rim.

5.2 Choice of Lens

The two lenses used in the experiment were the plano-convex and the aspheric[14], with focal lengths of 200mm and 1.49mm respectively. Initially, the plano-convex lens was used. This was an attractive alternative over the aspheric from time constraint perspective, since due to its long focal length, it could be placed outside the vacuum chamber. Since the ultimate objective of the experiment is to trap a particle in the vacuum, mounting the aspheric would require a specialised custom-made mount that would fit inside the vacuum chamber. Since the focal length is much greater than the diameter of the lens, the plano-convex lens is also well described by the Gaussian beam model, ensuring a predictable shape of the standing wave intensity maxima which do not let

[14] Mounted Geltech Aspheric Lens `C710TMD-C`, Thorlabs

the particle escape. In practice, trapping was not successful with the plano-convex. The reason for this before moving onto the aspheric lens was not analysed, but it was most likely due to insufficient intensity at the focus, not strong enough to support the particle.

Having a much smaller Rayleigh range, the aspheric lens produced a much tighter focus and eventually allowed to successfully trap the particle at the final stage of the experiment. Whilst there is always a solution where the beam and mirror surface curvatures match, the result derived in section 3.2, shows that a beam with small z_R has its focus coincide with the geometric focus of the mirror. This is highly favourable for when the RPSN from Rayleigh scatter suppression is considered. There is however one primary concern when considering this choice of lens for particle trapping. The particle is very sensitive to the gradient of the intensity. Since NA=0.53 for the aspheric, the paraxial approximation may no longer be valid. Hence, it is reasonable to question whether the Gaussian beam model is still applicable. It is not clear to what extent it affects the intensity profile of the beam, and testing this in a finite-element simulation would provide useful information.

5.3 Fibre Optics

The 1550nm seed laser generated a power output of about 50mW. Flow of power in the experiment was controlled and monitored using the two primary fibre optic components - the tap coupler and the circulator. The first tap connected to the seed laser was used to split the power of the laser between the two experiments being conducted simultaneously in the lab. When using the amplifier in the later experiments, this tap also ensured that the amplifier input was below maximum specified by the manufacturer[15]. Since the manual recommends an input between -10dBm and 16dBm, a 1:10 tap was selected to fit in the range. The 10% power end used when using the amplifier and the 90% was used for alignment purposes without the amplifier at the earlier stage of the project. A low-loss (1:1000) tap was added between the circulator and the collimator to help detect hidden power losses. It is worth mentioning that although the tap couplers were sold as ones with 1:10 or 1:1000 power splitting, the test sheets corresponding to individual devices used in the lab have differing losses as stated on the test sheets. This is due to imperfections during manufacture.

The third tap connecting the circulator and the measuring devices was inserted to use the photodetector and the power meter at the same time. The power meter provided a power readout from the back-reflection and allowed to measure the power output to determine whether it is within the recommended input range of the photodetector before it was connected. The linear

[15] BKTEL, Model no. `HPOA-S`

amplification regime of the photodetector used[16] saturates at 60μW. In anticipation of large mirror back-reflection, the 1:1000 tap was therefore selected. In the end, particles were trapped in the focus of the lens without the mirror in place, hence large back-reflections were not a problem; the back-reflected power was in the micro-range, but well below the saturation value. This meant that the low-loss end can be connected to the photodiode.

Laser power was amplified up to 4W with a minor loss of 0.8dB in the circulator. Optical fibres were cleaved[17] and spliced[18] with negligible loss introduced. The 29dB ports in the 1:1000 connecting to the collimator were used for power measurements. Since the circulator consists of polarisation dependent components, about -50dB of light passes through to the wrong port. Due to high laser power input, the -50dB channel allowed for about 10μW to pass through from the amplifier to the detection devices, effect of which was manifested as a fluctuating power reading in the μW range[19]. This power leakage served as a high-loss channel, allowing for an interferometric measurement of the Rayleigh back-scatter which passes through the same port. This is illustrated in figure 5.3.

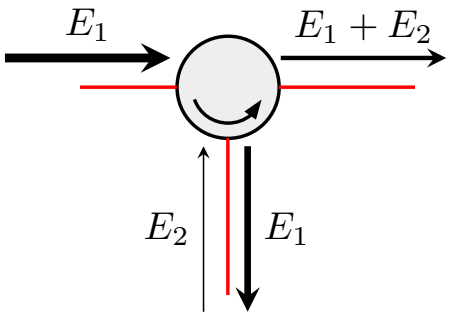

Figure 5.3: A diagram showing the circulator along with the fields which enter and leave its ports. The thickness of the arrows indicates the changing magnitude of field amplitudes at different ports.

Field E_1 corresponds to the laser leaving the amplifier and entering the circulator. The circulator directs the beam towards the trap site but a small fraction of light passes through the -50dB channel, serving as a reference signal. Light directed to the trap site interacts with the trapped particle causing it to Rayleigh scatter. Some of the scattered light is captured back into the collimator and it is what gives rise to field E_2. Field E_2 differs from E_1 by amplitude and phase which it acquires in the additional distance travelled, which will therefore depend on the position of the

[16] 200 MHz Photoreceiver series with InGaAs PIN Photodiode `HCA-S-200M`
[17] Fujikura fibre cleaver `CT-30`
[18] Fujikura fusion splicer, `FSM-185`
[19] Reading which is below the saturation threshold of the photodiode

particle. The two fields can then be written as,

$$\begin{aligned} E_1(t) &= A\cos(\omega t), \\ E_2(t) &= B\cos(\omega t + \phi(z)), \end{aligned} \tag{5.1}$$

where A and B are the field amplitudes[20] and z is the particle position in the trap along the beam axis. Field E_2 is then directed to the port connected to the detection devices, where it interferes with the reference signal E_1. This constitutes the *homodyne measurement* scheme; frequencies of the interfering signals are the same. In this setup, the photodiode measures the phase-sensitive signal,

$$V = |E_1 + E_2|^2 \propto A^2 + B^2 + 2AB\cos(\theta - \phi(z)) \tag{5.2}$$

where θ is the additional phase which the scattered light acquires travelling from the particle all the way back to interfere with the reference field. The interferometric signal could then by analysed to infer the particle's position in the trap. In the next section, an estimate was made of how much power is coupled back into the collimator for different focusing optics. The form of the signal and the random nature of the random phase θ is expanded on in section 6.2.5, needed for the development of the measurement model in the unscented Kalman filter.

5.4 Capturing Rayleigh Backscatter

Mie theory is concerned with modelling the scattering of plane waves from a spherical obstacle. Rayleigh scattering, as a limit to Mie theory, is a useful simplification when the electric field does not vary significantly across the particle. It is useful for the system considered in this project, since the nanoparticles used, with a radii of order 100nm, are much smaller compared to the wavelength used - 1550nm.

One way of obtaining intensity of Rayleigh scatter is by applying the *dipole approximation* to Mie theory. It can then be shown that the beam intensity I_0, at wavelength λ scattered by a small sphere of radius r and relative permitivity ϵ_r at a certain scattering angle θ corresponds to a scattered intensity,

$$I(R,\theta) = I_0 \left(\frac{2\pi}{\lambda}\right)^4 \left(\frac{\epsilon_r - 1}{\epsilon_r + 2}\right)^2 r^6 \left(\frac{1+\cos^2(\theta)}{2R^2}\right), \tag{5.3}$$

where R is the distance between the scatterer and the observation point. Factor of $1 + \cos(\theta)^2$ captures all the behaviour of the scattered intensity with the changing scattering angle; the intensity is maximum for at $0°$ and $180°$ with respect to the incoming beam and minimum at $\pm 90°$. This was illustrated in figure (5.4), which shows the Rayleigh scattering from particle in a gen-

[20] Note that the values of A and B are different at different ports in figure 5.3

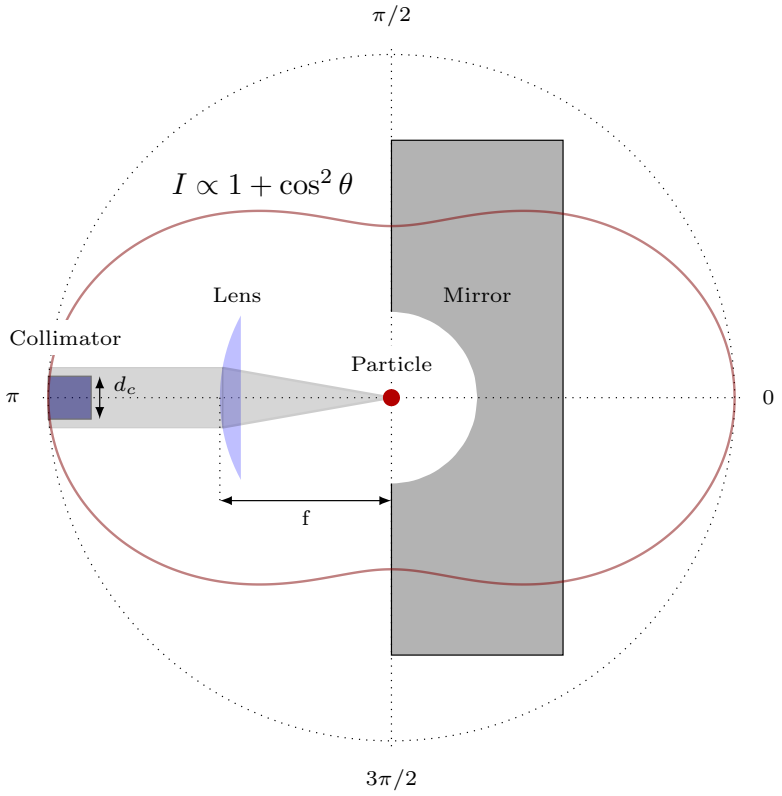

Figure 5.4: Diagram demonstrating the optical arrangement near the mirror, along with Rayleigh-scattered light from a trapped nanoparticle at the focus of the incoming beam. Scattered light is collimated to the left by the plano-convex lens in the same way it is focused in the reverse direction. The crimson line shows the magnitude of the scattered intensity (see equation (5.3)) with respect to the scattering angle.

eral optical arrangement considered for this project. Equation (5.3) can be integrated over the solid angle to obtain the scattered intensity in a given direction. In particular, it can be used to determine the expected power from Rayleigh backscatter. Assuming that the backscattered light remains collimated after passing through the lens, in a perfectly aligned arrangement, the intensity collected by the collimator is equivalent to considering the collimator at the position of the lens. Intensity collected back into the collimator is therefore given by the integral of equation (5.3) for a solid angle Ω_c spanned by the diameter of the collimator d_c at focal length f of the lens,

$$I_{\text{collected}} = \underbrace{\frac{I_0}{2}\left(\frac{2\pi}{\lambda}\right)^4\left(\frac{\epsilon_r - 1}{\epsilon_r + 2}\right)^2 r^6}_{C}\int_{\Omega_c} \mathrm{d}\Omega \left(\frac{1 + \cos^2(\theta)}{R^2}\right). \tag{5.4}$$

The solid angle in cylindrical coordinates can be written as,

$$\mathrm{d}\Omega = R^2 \mathrm{d}\phi(\cos(\theta)), \tag{5.5}$$

where $d\phi$ is the rotation angle about z direction. The system has cylindrical symmetry about the axis of the incoming beam (z direction), so $d\phi$ will give a trivial integral and $z = -f$ is constant.

For $f \gg d_c$ the approximation $\sin(\theta) = d_c/2f \approx \theta$ is also valid. Hence the integral from (5.4) becomes,

$$I_{\text{collected}} \approx C \int_0^{2\pi} \mathrm{d}\phi \int_{\pi+d_c/2f}^{\pi-d_c/2f} \mathrm{d}(\cos(\theta)) \left(1+\cos(\theta)^2\right) = 4\pi C \left[\cos(\theta) + \frac{\cos(\theta)^3}{3}\right]_{\pi}^{\pi-d_c/2f} \tag{5.6}$$

The collimator[21] used in the experiment has a diameter of 14.9mm. For $f = 200$mm lens, and a 1W Gaussian beam focused down to a spot size of $w_0^2 = (10\mu\text{m})^2$ corresponding to the beam waist, trapping a nanoparticle of fused silica ($\epsilon_r = 2.25$) of radius $r = 200$nm the intensity of the incident beam is $I_0 = 10^{10}$ Wm^{-2}. From equation (5.6), the backscatter power collected by the collimator in this case is,

$$P_{\text{collect}} = \left[\pi \left(\frac{d_c}{2}\right)^2\right] I_{\text{collect}} = 2.27 \times 10^{-11}\text{W} \tag{5.7}$$

Assuming that the beam retains its Gaussian profile after passing through the aspheric lens, a similar calculation to the above can be done. A short derivation provided in the Appendix gives an estimate of the waist as a consequence of the paraxial approximation. The result of the derivation given in equation (3.15) then gives an estimate of $w_0^2 = (0.99\mu\text{m})^2$. Again taking the power coming out the collimator to be 1W, giving $I_0 = 10^{12}\text{Wm}^{-2}$. In contrast to the above calculation, the aspheric lens underfills the collimator with backscattered light. This is equivalent to setting $d_c = d_{\text{aspheric}} = 2.1$mm, giving,

$$P_{\text{collect}} = \left[\pi \left(\frac{d_{\text{aspheric}}}{2}\right)^2\right] I_{\text{collect}} = 138\text{nW} \tag{5.8}$$

The photodetector used[22] has a noise equivalent power of $5.2\text{pW}/\sqrt{\text{Hz}}$. Both of the estimates exceed this value, indicating that the lenses are suitable for detecting Rayleigh backscatter.

[21] Triplet Collimator `TC18APC-1550`, purchased from Thorlabs
[22] 200 MHz Photoreceiver series with InGaAs PIN Photodiode `HCA-S-200M`

5.5 Trapping the Nanoparticle

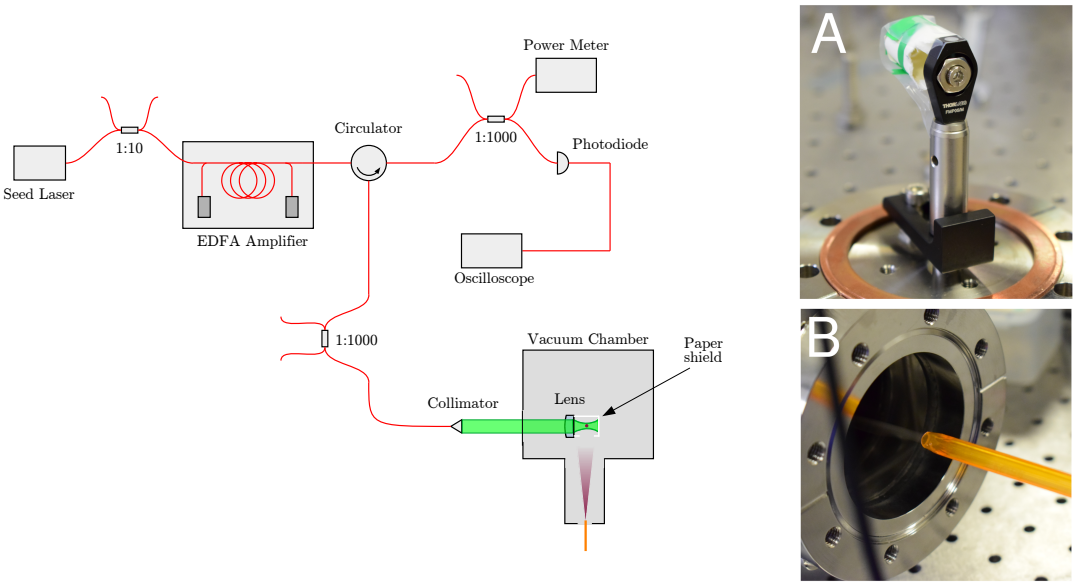

Figure 5.5: Final experimental setup used for trapping the nanoparticle. Red lines represent optical fibres. The laser beam (green) enters the vacuum chamber through a glass window. The plastic tube (orange) was used to spray the nanoparticles into the vacuum through the side vacuum door. The white line stopping the laser beam around the lens represents the cross section of a cylindrical paper shield with a small opening on the side used to contain the spread of the nanoparticle aerosol. (A) Picture of the lens with the paper shield attached. (B) Picture taken of the aerosol spray into the vacuum chamber during a trapping attempt.

Trapping of the nanoparticle was achieved using the setup in figure (5.5). The particles were loaded into the trap site with a commercial nebuliser; sprayed in using a narrow plastic tube through the side door of the vacuum chamber. Initially, the nebuliser contained a highly diluted solution of silica nanoparticles suspended in ethanol [38]. However, this solution did not seem to produce a good aerosol with the nebuliser used[23]. The diluting liquid was replaced with distilled water which allowed for successful trapping. Whether a particle was trapped successfully was indicated by the signal waveform generated by the oscilloscope. The power spectral density (PSD) was also generated live from the time samples (see figure 5.6).

In the left of figure (5.6) there is a sharp spike at 0Hz, which usually corresponds to a DC offset. The periodic peaks of the signal's power spectral density on the right of figure (5.6) arise as a result of the shape of the PSD corresponding to particle's position S_{xx} encoded in the signal of the form in equation (5.2). Rigorous analysis of the shape shown in figure 5.6 is non-trivial [31] if one is to accurately deduce more than just basic quantities. However, the signal PSD can be inspected to easily obtain the trap frequency as the peaks are separated by Ω_z. The width of the peaks also indicates the magnitude of the local pressure. The minimum attainable pressure with

[23] OMRON MicroAir U22

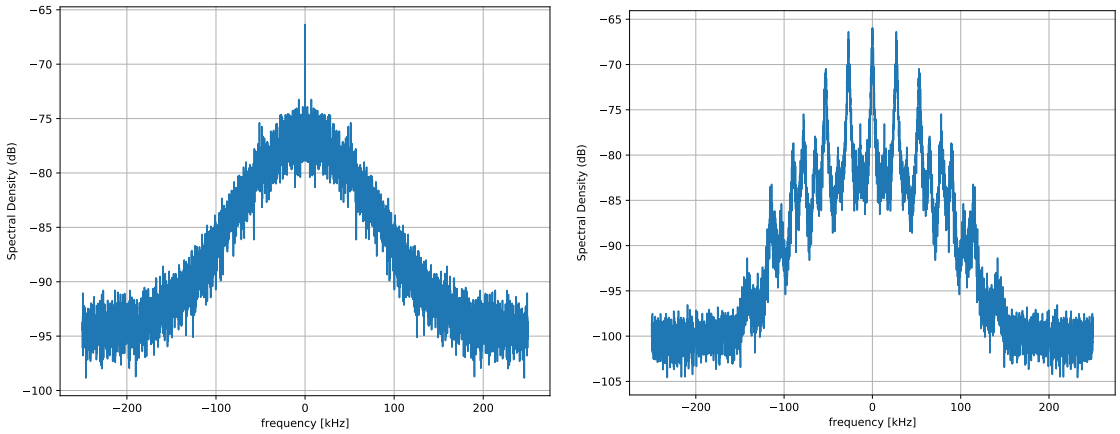

Figure 5.6: Snapshots of the PSD obtained during trapping of the particle at different pressures **Left** Pressure 310 mbar measured with a hybrid Pirani gauge (`Pfeiffer ITR90`) **Right** Pressure $\sim$ 0.1 mbar. The snapshot was taken during a time when the pressure gauge was not available.

the vacuum pump used (Edwards nXDS6i) is 0.020 mbar, and the emergence of peaks indicates significantly lower pressure than in the figure on the left. Width of the individual peaks gives the damping rate, from which pressure can be estimated. Using results from [15] the pressure can be estimated to be about 0.1mbar.

6 Site Hopping

Since the loading process utilises the nebuliser, it does not allow for a precise control of the initial position of the particle in the trap. Once the aerosol is ejected, the particle follows a random walk towards the trap site. The particle can therefore land at a random site within the trap. However, precise control over particle position is required as Rayleigh scatter suppression would only occur for a particle trapped in a maximum in the vicinity of the geometric focus of the mirror.

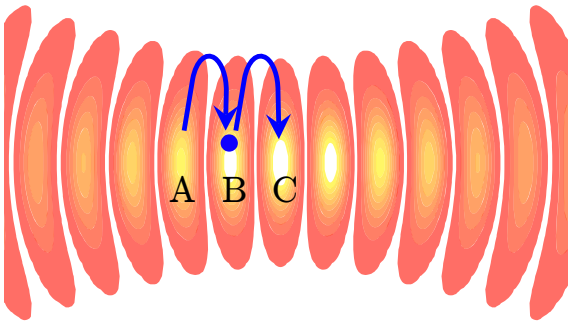

Figure 6.1: Zoom-in diagram of standing wave intensity maxima near the primary maximum, with a particle (blue circle) trapped at site B. In the diagram, trap site C is the geometric focus of the hemispherical mirror, where Rayleigh scatter suppression would occur. The particle is made to move ballistically from site A to B to C by modulation of intensity.

In this part of the project ballistic transfer scheme is designed to overcome this problem. The problem and the intended transfer is illustrated in figure 6.1. Motion of the particle is initially excited, after which the laser is switched off for a short period of time. This allows the particle to follow a parabolic path under the influence of gravity, akin to throwing a macroscopic object. Ballistic transfer from one site to another is simulated by first initiating the state of the particle (position and velocity) in 2D, at a random site with the centre maximum of the Gaussian beam standing wave with zero velocity. The particle in the simulation is subject to forces due to intensity gradient of the beam and random kicks provided by the environment at atmospheric pressure. State of the particle is evolved in time by applying the Euler-Maruyama method to the stochastic differential equation which governs the dynamics of the particle (See Appendix section 8.1). The effective intensity is encoded as $I^{'}(t,x) = M(t)I(t,x)$ where $I(t,x)$ is the intensity of the incident beam interfering with its retro-reflection and $M(t)$ is the modulation function controlled by the AOM. Primary focus of this part of the project is to transfer the nanoparticle to an adjacent maximum of choice with high probability of success. In the first approach in tackling the problem, the modulation function $M(t)$ allows for transfer of about 2/3 of simulated particles into adjacent maxima without control of the direction, (see figure (6.2)) and it is implemented as follows:

1. Allow the simulated particles to thermalise or initiate a thermalised data set, after which turn on $M(t)$.

2. Parametrically excite the particles' motion for time T using the sinusoidal function $M(t) = 1 + \beta \sin(\Omega_m t)$ where Ω_m is the modulation frequency.

3. After time T, turn the laser off for a duration of τ. Equivalently, $M(t) = 0$ for $T \leq t < T + \tau$.

4. After time τ turn the laser back to normal mode of operation; $M(t \geq T + \tau)$ to let the particles thermalise.

In the above, $\Omega_m = 4\pi \times 793\text{kHz}$ (about twice as large as the trap frequency Ω_z) and β, T, τ are adjustable parameters. Figure (6.2) shows unacceptable accuracy, succeeding only about a third of the time in transferring the particle to the site of choice. The simplistic approach presented above has to be refined in order to reach a greater degree of accuracy. The remainder of this section explores this possibility by utilising a powerful data analysis technique.

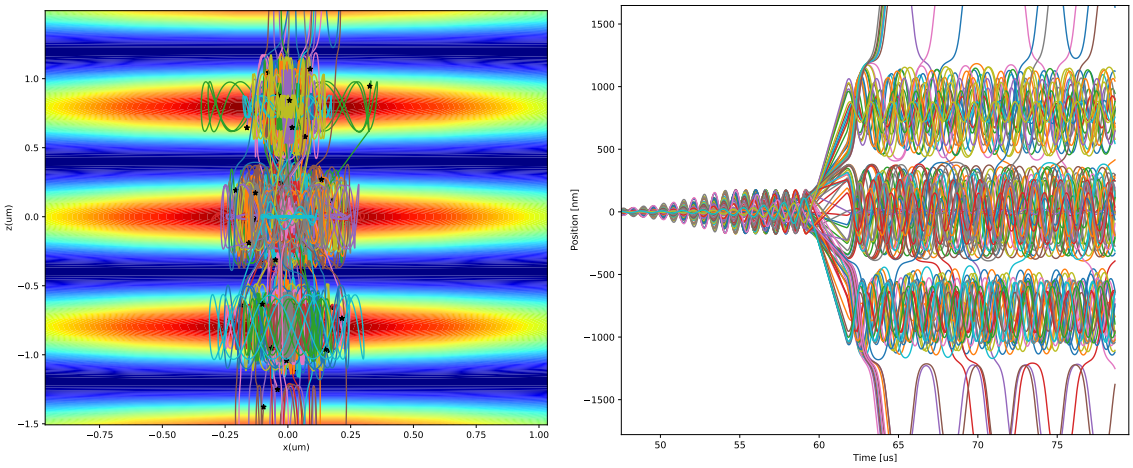

Figure 6.2: Simulated trajectories for 100 nanparticles with $\beta = 0.3, T = 30\mu\text{s}$ and $\tau = 2.5\mu\text{s}$. The damping rate, which controls the rate at which random kicks are applied to the particle was set to $\Gamma = 100\text{kHz}$. **Left** Intensity contour plot overlapped with particle trajectories in the x-z plane. **Right** z-coordinate plotted against time

6.1 Problem Statement

As evident by the results shown above, the direction of the particle throw cannot be controlled. Particle is initiated at a random position which captures the fact that it behaves stochastically. Although it exhibits damped harmonic motion, it is subject to a random force and its initial position is unknown. It can be seen in figure (6.2) that setting T and τ to a constant value yields

only about a 1/3 to transfer to the correct maximum. If however, the position of the particle in the trap could be deduced, the parameters could be adjusted to let the particle go at a time such that it reaches the preferred adjacent maximum with sufficiently high probability. This can be achieved by analysing the data collected live during trapping with a device fast enough to perform real-time analysis. Tracing the particle's position in the trap would then allow to determine the suitable parameters needed to transfer the particle. The following sections explore the method of inferring particle position within the trap using the measured signal, and using this information to select an appropriate release time. The primary tool used to achieve this is a statistical algorithm called *the Kalman filter*. The linear Kalman filter is fully discussed in the section 3.6 as it forms a basis for more general implementations. For reasons outlined in section 3.7, the modified version of the Kalman filter had to be used - *the Unscented Kalman filter* (UKF). What follows is a detailed description of how the problem was encoded for the operation of the UKF.

6.2 Implementation

6.2.1 State Representation

As the primary quantity of interest is the current position and direction of travel, the state could be chosen to be represented as a 2-dimensional vector of position and velocity along the beam axis. However, the path length between the particle and the reference signal fluctuates due to mechanical and thermal vibrations in the fibre. Dynamics of this random fluctuating phase θ in the fibre pollute the measurement hence their description needs to be included in the model. The state was therefore represented as a 4-component vector,

$$x_k = \begin{bmatrix} z \\ \dot{z} \\ \theta \\ \dot{\theta} \end{bmatrix}_k . \tag{6.1}$$

where subscript k indicates the discrete time step. The corresponding covariance matrix then follows to be represented as,

$$\mathbf{P}_k = \begin{bmatrix} \sigma^2_{zz} & \sigma^2_{z\dot{z}} & \sigma^2_{z\theta} & \sigma^2_{z\dot{\theta}} \\ \sigma^2_{\dot{z}z} & \sigma^2_{\dot{z}\dot{z}} & \sigma^2_{\dot{z}\theta} & \sigma^2_{\dot{z}\dot{\theta}} \\ \sigma^2_{\theta z} & \sigma^2_{\theta\dot{z}} & \sigma^2_{\theta\theta} & \sigma^2_{\theta\dot{\theta}} \\ \sigma^2_{\dot{\theta}z} & \sigma^2_{\dot{\theta}\dot{z}} & \sigma^2_{\dot{\theta}\theta} & \sigma^2_{\dot{\theta}\dot{\theta}} \end{bmatrix}_k , \tag{6.2}$$

where σ^2_{AB} is the covariance defined as $\mathrm{E}[(A - \mathrm{E}[A])(B - \mathrm{E}[B])]$[24].

[24] 'E' denotes the expectation value as usual

6.2.2 Initial Values

Initial position and velocity are unknown however UKF can still perform effectively with only a rough estimate. For convenience, all results were obtained with the initial position set to the actual starting site of the particle and zero velocity. Phase is also initialised at 0, which was its actual initial value. No knowledge of $\dot{\theta}$ is assumed hence the initial a posteriori state takes the form,

$$\hat{\mathrm{x}}_0 = \begin{bmatrix} 0 \\ 0 \\ 0 \\ 0 \end{bmatrix}_0 . \tag{6.3}$$

which can be compensated for by setting a sufficiently high initial error. In general, a high uncertainty in the initial state causes the filter to be prone to divergence. This was avoided in this study by assuming a good knowledge of the initial state. A more realistic scenario is discussed in more detail in section 6.4. The covariance of the initial state is set to be uncorrelated among the state components. This is not accurate in general but is sufficient for the filter input. As the filter progresses, correlation will develop naturally between different state components as described by the system dynamics. From system dynamics, no cross correlation is expected between the phase and position and their respective rate of change, hence the initial covariance was represented as a block matrix,

$$\hat{\mathbf{P}}_0 = \begin{bmatrix} \hat{\mathbf{P}}_z & \mathbf{0} \\ \mathbf{0} & \hat{\mathbf{P}}_\theta \end{bmatrix}_0 , \tag{6.4}$$

where $\hat{\mathbf{P}}_z$ and $\hat{\mathbf{P}}_\theta$ are 2×2 covariance matrices describing $(z, \dot{z})$ and $(\theta, \dot{\theta})$ respectively, $\mathbf{0}$ is a 2×2 matrix with zeroes in all elements and $\hat{\mathbf{P}}_0$ is a 4×4 initial covariance matrix describing the entire system. A discussion now follows on how the sub-matrices were chosen to represent the initial covariance.

The position of the particle along the beam axis is known to be somewhere around $(0 \pm 10)\mu$m with similar magnitude of error in the velocity. Hence the initial covariance matrix was first set to,

$$\hat{\mathbf{P}}_z = \begin{bmatrix} 1 & 0 \\ 0 & 1 \end{bmatrix}_0 \times 10^{-10}. \tag{6.5}$$

Despite an accurate representation of the initial posterior knowledge, a value too large for the initial covariance can cause the filter to diverge [32]. It is appropriate to set the initial covariance to be artificially small to prevent the filter from diverging[25]. This means that the filter will under-

[25] If the discrepancy between the actual site and initial site estimate is too large, the filter will still diverge even if the error is underestimated.

perform in the initial set of iterations, but the divergence can nonetheless be avoided[26]. Indeed, this was the case for the choice in equation (6.5) and a lower value for the covariance was needed. Instead the following choice was used,

$$\hat{\mathbf{P}}_z = \begin{bmatrix} 1 & 0 \\ 0 & 1 \end{bmatrix}_0 \times 10^{-13}. \tag{6.6}$$

Here in equation (6.7) correlation is expected, but the initial covariance was assumed to be uncorrelated. This is sufficient for the initiation but is be accounted for later when modelling the process noise.

A similar problem arose when choosing the initial phase covariance is modelled in a similar fashion. At first the initial variance was assumed to be equal to $(\pi/2)^2$ given no knowledge of the phase since $\theta = 0 \pm \pi/2$. Again assuming no initial correlation, the phase covariance was represented as,

$$\hat{\mathbf{P}}_z = \begin{bmatrix} 1 & 0 \\ 0 & 1 \end{bmatrix}_0 \times \left(\frac{\pi}{2}\right)^2. \tag{6.7}$$

However, this led to divergence in many cases hence a value much smaller than one was chosen to represent the initial covariance instead. The phase drift is a measurable quantity hence its accurate initial knowledge is not unrealistic (See section 6.4). The overall system covariance $\hat{\mathbf{P}}_k$ was then constructed as in equation (6.4).

6.2.3 System Dynamics Model

Position z and phase θ do not influence each other dynamically. The following description considers the development of the dynamics model separately for the two quantities and combines them at the end.

As outlined in section 3.4 the particle follows harmonic motion modulated stochastically with random kicks provided by the environment,

$$\ddot{z}(t) + \Gamma \dot{z}(t) + \Omega_z^2 z(t) = \frac{F(t)}{m} \tag{6.8}$$

The random force is modelled as process noise as it is a form of unaccountable influence on the dynamics of the particle. This is a linear model hence it can be modelled identically to the standard linear Kalman filter. Firstly, the second order differential equation in (6.8) is converted

[26] Underestimating the initial position state can also introduce global bias. However, this is not a problem in this study since only direction of travel and velocity magnitude are relevant.

to a 2 dimensional first order system,

$$\dot{x} = \begin{bmatrix} z \\ \ddot{z} \end{bmatrix} = \begin{bmatrix} 0 & 1 \\ -\Omega^2 & -\Gamma \end{bmatrix} \begin{bmatrix} z \\ \dot{z} \end{bmatrix} = \mathbf{A}x. \tag{6.9}$$

Equation (6.9) has to be transformed from the continuous state space model to a discrete time based model. In other words, given an equation of the form $\dot{x} = \mathbf{A}x$ we wish to find matrix $\mathbf{F}$ containing a time step Δt that will evolve or predict the state recursively for the next time step $k \mapsto k+1$,

$$x_{k+1} = \mathbf{F}x_k. \tag{6.10}$$

In general, for a multi-dimensional linear system, the solution is given by,

$$\mathbf{F} = e^{\mathbf{A}\Delta t} = \mathbf{I} + \mathbf{A}\Delta t + \frac{(\mathbf{A}\Delta t)^2}{2!} + ... \tag{6.11}$$

This can also be seen to arise by considering the approximation,

$$\begin{aligned} \dot{x} = \mathbf{A}x(t) &\approx \frac{x(t+\Delta t) - x(t)}{\Delta t}, \\ x(t+\Delta t) &\approx (\mathbf{I} + \mathbf{A}\Delta t)x(t), \end{aligned} \tag{6.12}$$

where the term in parentheses is the approximation used for the matrix $\mathbf{F}$,

$$\mathbf{F} = \begin{bmatrix} 1 & \Delta t \\ -\Omega_z^2 \Delta t & 1 - \Gamma\Delta t \end{bmatrix}. \tag{6.13}$$

In the case that $1 \gg \Omega_z^2\Delta t, \Gamma\Delta t$ the approximation (6.13) would suffice as the description of the dynamics, however this is not the case and therefore the full exponential has to be used. When fully expanded, the dynamics matrix for the particle position becomes,

$$\mathbf{F}_z = \frac{e^{-\Gamma\Delta t}}{\Omega} \begin{bmatrix} \Omega\cos(\Omega\Delta t) + \Gamma\sin(\Omega\Delta t) & \sin(\Omega\Delta t) \\ -\Omega_z^2\sin(\Omega\Delta t) & \Omega\cos(\Omega\Delta t) - \Gamma\sin(\Omega\Delta t) \end{bmatrix}, \tag{6.14}$$

where $\Omega = \sqrt{\Omega_z^2 - \Gamma^2}$.

Thermal drift in the fibre translates to Brownian-like motion of the phase offset. Phase θ can be modelled to behave as a damped harmonic oscillator with a stochastic driving term where the frequency of oscillation goes to zero. It can be described by the differential equation,

$$\ddot{\theta}(t) + \gamma\dot{\theta}(t) = \gamma(t), \tag{6.15}$$

where $\gamma(t)$ is a stochastic (*Weiner*) process. Following the same steps as for the dynamics of the

particle, the phase's dynamics are governed by,

$$\mathbf{F}_\theta = \begin{bmatrix} 1 & \frac{e^{-\gamma\Delta t}}{\gamma} \\ 0 & e^{-\gamma\Delta t} \end{bmatrix}. \tag{6.16}$$

The recursive evolution of the 4-dimensional state vector is then fully described by the matrix,

$$\mathbf{F} = \begin{bmatrix} \mathbf{F}_z & \mathbf{0} \\ \mathbf{0} & \mathbf{F}_\theta \end{bmatrix}, \tag{6.17}$$

similarly to how the initial covariance matrix was constructed. In the standard Kalman filter, $\mathbf{F}$ would then be used to find the a priori estimate,

$$\mathrm{x}_{k+1} = \mathbf{F}\hat{\mathrm{x}}_k, \tag{6.18}$$

however UKF takes functions as inputs for the system dynamics and measurement as it generalises to nonlinear systems, meaning that a small alteration is required to model the system dynamics. Namely, a function is programmed such that,

$$f((\mathscr{X}_i)_k) = \mathbf{F}(\mathscr{X}_i)_k = (\mathscr{Y}_i)_k. \tag{6.19}$$

where $(\mathscr{X}_i)_k$ is the ith sigma point at time step k. Notice that the random force $F(t)$ was not included in the description of the dynamics. This is because the filter will instead compensate by adding uncertainty to the state of the particle at every time step in the form of process noise. Formulation of the process noise is the subject of the next section.

6.2.4 Modelling Process Noise

It was mentioned in the previous section that in order to accurately model the process noise, the covariance of the state estimate has to include correlated terms. This can be achieved using the *piecewise noise model* in which the noise varies between different time steps, but is assumed constant within the duration of the time step. In context of the particle moving in the trap, the random force is assumed to provide constant acceleration kicks, but random between different time steps. In the standard Kalman filter this would be represented as,

$$\begin{bmatrix} \frac{1}{2}\Delta t^2 \\ \Delta t \end{bmatrix} \mathrm{w}_k, \tag{6.20}$$

as an added term to the state extrapolation equation (as described in section 3.6). From equation (6.20) the process covariance is then constructed with,

$$\mathbf{Q}_z = \mathrm{E}\left\{ \begin{bmatrix} \frac{1}{2}\Delta t^2 \\ \Delta t \end{bmatrix} \mathrm{w}_k \left(\begin{bmatrix} \frac{1}{2}\Delta t^2 \\ \Delta t \end{bmatrix} \mathrm{w}_k \right)^{\mathrm{T}} \right\} = \sigma_z^2 \begin{bmatrix} \frac{\Delta t^4}{4} & \frac{\Delta t^3}{2} \\ \frac{\Delta t^3}{2} & \Delta t^2 \end{bmatrix}. \tag{6.21}$$

In equation (6.21) σ^2 is the process variance, serving the purpose of a tuning parameter. It can be estimated by considering how the random force arises but it can also simply be tuned during simulation. An appropriate value of the process variance is necessary for the filter to work. The values chosen for the operation of the filter $\sigma_z^2 = 10^{12}$ was found by tuning such that the best performance was achieved relative to the true trajectory. In a realistic scenario the true trajectory is not available but the choice found in simulations can be used or a theoretical estimate could be made.

The above description was concerned with the position and velocity, but it can by equally well applied as a model of the process variance in the phase. The overall process variance was expressed as a block matrix,

$$\hat{\mathbf{Q}} = \begin{bmatrix} \mathbf{Q}_z & \mathbf{0} \\ \mathbf{0} & \mathbf{Q}_\theta \end{bmatrix}, \tag{6.22}$$

where $\mathbf{Q}_\theta$ where taken to have process variance of $\sigma_\theta^2 = 10^{25}$, which was found to perform well.

6.2.5 Signal Simulation and the Measurement Model

As discussed in section (5.3), the experiment generates an interferometric signal of the form,

$$V \propto A^2 + B^2 + 2AB\cos(\theta - \phi(z)). \tag{6.23}$$

Phase $\phi(z)$ is sensitive to the axial position z[27] and θ is some phase offset. $\phi(z)$ is modelled by the linear relationship $\phi(z) = \kappa z$ where κ is some phase sensitivity dependent on the optical geometry and the wavelength of the laser used. A collimated beam has its phase evolve at a rate equal to the wavenumber k, but the Gouy shift of the highly focused laser beam slows the evolution of the phase. However, as the experiment concerns a backscatter geometry, not all light experiences the Gouy shift. Rayleigh backscattered light is not highly focused and its phase evolves at the regular rate k (See figure (6.3)). The sensitivity κ for the interferometric signal can then be approximated as the phase for a round trip as, [31]

[27] This is due to the optical arrangement - it is symmetric about the beam axis and the laser field induces a dipole in a transverse direction. The intensity coupled back into the collimator by a transversely displaced particle is mostly invariant as the intensity pattern ($I \propto 1 + \cos^2(\cdot)$) is aligned along the beam axis.

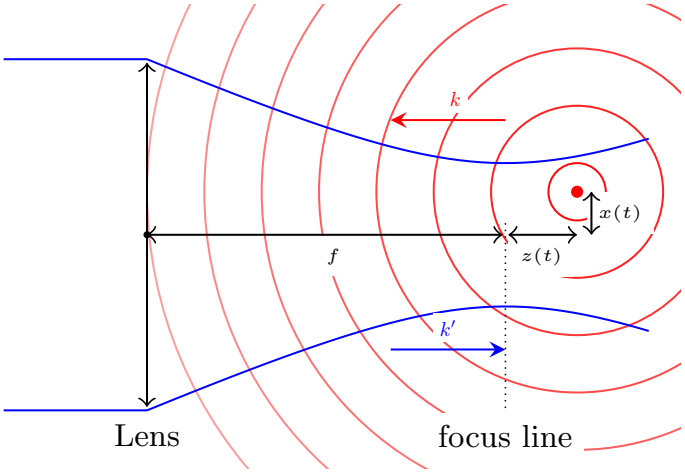

Figure 6.3: Cross section of the simulated geometry. Blue line indicates the outline of the laser beam . The red node indicates the position of the nanoparticle in the trap. The red lines indicate the wavefronts of Rayleigh scattered light moving radially. The rates of phase evolution are also indicated, according to the respective colours. Note that the particle doesn't scatter with equal intensity in all directions (as in section 5.4) but nonetheless it scatters radially.

$$\kappa \approx k + k' = 2k + \frac{1}{z_R}, \tag{6.24}$$

where k' is the Gouy shifted rate of phase evolution of a Gaussian laser field. Phase θ encodes the additional distance that the laser field travels to reach the particle; Choosing the focus of the laser as the reference point, then $\theta = [f + (...)]$. f is the focal length of the lens in free space and the term in parentheses is the sum of the distance from the lens to the collimator and the extra distance that the field traverses within the optical fibre. Due to thermal and mechanical fluctuations, this extra distance within the fibre is subject to fluctuations. This means that θ can be re-written as some constant corresponding to a fixed distance and a random drifting term,

$$\theta = -\frac{\pi}{2} + \theta_r(t) \tag{6.25}$$

where $-\pi/2$ was chosen for convenience. It then follows that the signal in equation (6.23) can be written as,

$$V = V_0 \sin(\kappa z(t) + \theta_r(t)), \tag{6.26}$$

where the additive constant terms in equation (6.23) were ignored as they only introduce an invariant offset to the signal. The phase $\theta_r(t)$ encompasses the randomly fluctuating and drifting nature of the phase and is the state variable evolved as described in section 6.2.3. V_0 is the amplitude of the signal which depends on the sensitivity of the photodiode.

Equation (6.26) gives the expected form of the signal to come out from the experiment. For

the purpose of the study, the observed signal (or the measurement $(\mathscr{Z}_i)_k$) was modelled as,

$$(\mathscr{Z}_i)_k = h((\mathscr{Y}_i)_k) = V_0 \sin(\mathbf{H}(\mathscr{Y}_i)_k) + V_G, \tag{6.27}$$

with V_G being Gaussian white noise. V_G was chosen to model the measurement noise in the experiment. Quantity $\mathbf{H}(\mathscr{Y}_i)_k$ recovers the simulated measurement in equation (6.26). Matrix $\mathbf{H}$ acts on the first and third vector component of the ith sigma point at time step k $(\mathscr{X}_i)_k$ transformed by function $f(\cdot)$ and is simply given by,

$$\mathbf{H} = \begin{bmatrix} \kappa & 0 & 1 & 0 \end{bmatrix}. \tag{6.28}$$

6.2.6 Choice of Sigma Points

The choice of sigma points boils down to selecting appropriate parameters for the Van der Merwe's scaled sigma point algorithm, as explained in section 3.7. This choice however is not well established and largly relies on trial and error choices and choices motivated by literature. Choices made for the simulation performed in this study are summerised in table 1. α controls the spread of sigma points and its choice can be motivated by the shape of the distorted non-Gaussian distribution. In other words, if the distribution is clustered close to the mean a small value of α close to zero would be an appropriate choice. The literature indicates that the choice $\beta = 2$ is optimal if the components of the state vector are Gaussian distributed, which is a good description for the position and velocity of the particle.

Parameter	Function	Suggested Value	Chosen value
α	controls the spread of sigma points	$0 \leq \alpha \leq 1$ [28, 33]	0.1
β	incorporate prior knowledge of the state components	2 [28, 33]	2
κ	secondary scaling parameter for the sigma points	0 [33],$3 - n$ [28]	1

Table 1: Parameters for the Van der Merwe's scheme of sigma point selection. n in this case is the dimension of the state vector.

6.3 Final Results and Analysis

Inclusion of the Unscented Kalman filter requires a significant change to the algorithm developed for site transfer, presented at the beginning of section 6. In this section, the development of the modified algorithm for site transfer is presented along with all the relevant results obtained along the way.

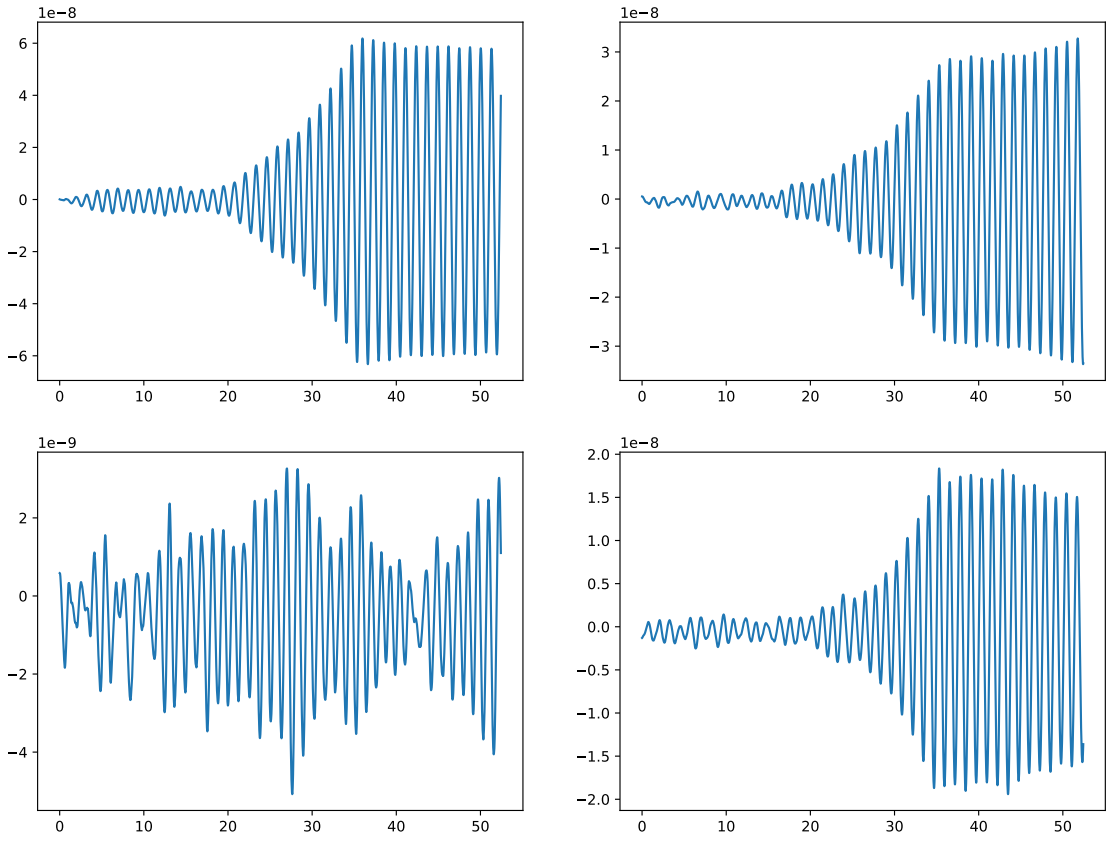

Figure 6.4: Position in m against time in µs. Four particle trajectories during the excitation period. Different particles respond differently to excitation depending on their state before the excitation. Note the order of magnitude on the vertical axis of the bottom-left plot relative to the others.

The two initial steps of the algorithm remain unchanged - the initiated particle is allowed to thermalise after which the intensity modulation function is switched on. Figure (6.4) shows the effect of excitation on the position of the particle in 4 different initial states[28]. The particle responds differently to excitation which is relevant for the application of the Kalman filter described below.

Particle's motion in bottom-left figure (6.4) is considered not well-behaved compared to the other three plots. In the other plots and in most cases, the particle's amplitude of oscillation is relatively high and their motion is thermalised prior to the excitation period. This led to a smooth

[28] State in this case means axial positions and velocities akin to the description of Kalman filters developed in the previous section

transition to an excited and mostly harmonic state of motion. The particle in the bottom-left had a relatively low spread in position and its motion was swamped by random kicks from the environment prior to excitation by intensity modulation. As a result, the particle did not respond well to excitation and its motion did not transition to a well-behaved harmonic state. This could have been caused by the constant 20μs period, chosen to allow the particle to thermalise which may not be enough time in all cases. This feature is likely to be unique to a simulation scenario, but it is still worth mentioning as it affects the results presented below.

The UKF was applied to a well-behaved and a badly-behaved trajectory of the particle, with results shown in figures (6.5) and (6.6) respectively. The results can be further improved using a smoothing algorithm, but this wasn't done as it requires additional computation time.

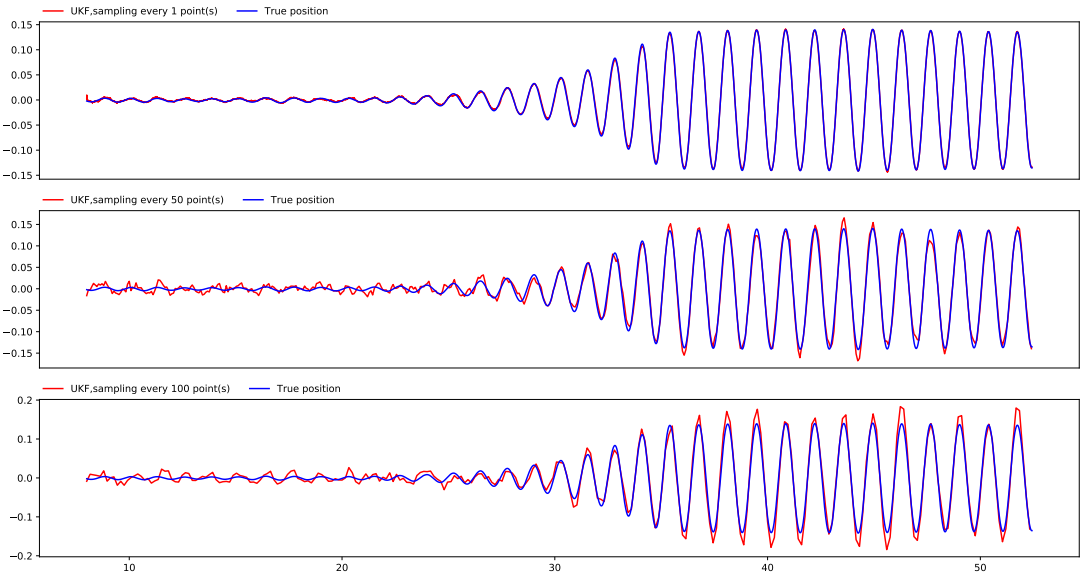

Figure 6.5: Position z in μm against time in μs. Position tracking of a well-behaved trajectory with the signal simulated for a 44.4μs period for different sample size per μs. The simulated signal consists of 22768 points in the highest resolution case. The top graph hides the inferred Kalman trajectory of the particle as it perfectly traces the true trajectory.

Both positions were successfully tracked without divergence, but showing vastly different performance depending on the behaviour of the trajectory. In the well-behaved case of figure (6.5) position is accurately tracked during, and after excitation period showing a small depreciation in accuracy for decreasing sample sizes. The filter performs better for the excitation period because the greater amplitude of oscillation increases the signal-to-noise ratio, making the measurement noise less significant. When sampling fewer points per microsecond, the filter only performs well after excitation. However, this is not an issue as UKF is to be applied after excitation. For the purpose of the simulation, the process variance was tuned to perform well in well-behaved cases.

In the case of figure (6.6), in which the trajectory of the particle is considered not well-behaved,

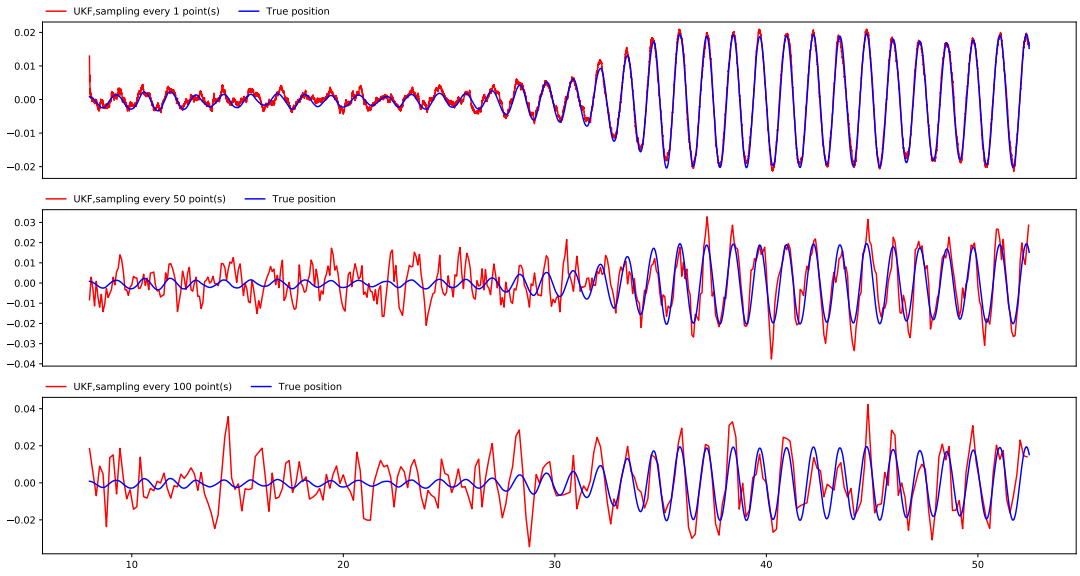

Figure 6.6: Position z in μm against time in μs. Position tracking of a badly-behaved trajectory with the signal simulated for a 44.4μs period for different sample size per μs. The simulated signal consists of 22768 points in the highest resolution case.

the filter can still track the position accurately at highest resolution. The decrease in accuracy is more apparent for lower sampling numbers per microsecond. In this case, when fewer points are sampled per μs the filter no longer is able to track the position as the noise power is of similar magnitude to the signal containing the information about the position. It is worth noting that results shown in figure (6.6) were generated using the same process variance as in figure (6.5). In fact, the accuracy of the filter could have been significantly improved if the process variance was re-tuned. However, the information on whether the particle behaves well or not is not experimentally accessible prior to the application of the filter. Since the simulations show that the particle behaves well in most cases, it is assumed that it is the best choice to tune the process variance for for the well-behaved case which will yield the highest accuracy in most cases of particle trapping.

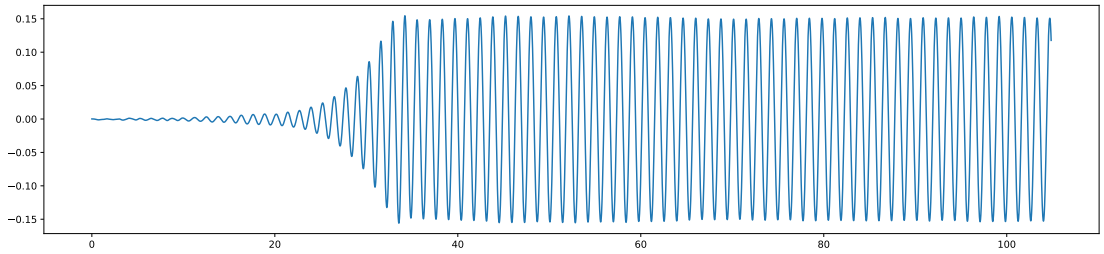

Figure 6.7: Position in μm against time in μs. The particle was excited for a duration of 15μs with the excitation parameter $\beta = 0.2$ after which it is allowed to relax. The damping rate $\Gamma = 50$kHz. The graph shows that the harmonic motion of the particle can persist for over 60μs.

In order to transfer the particle to an adjacent site of choice, the following alteration was made to the original algorithm. Firstly, apply the filter to a small time window of the signal. It can be seen in figure (6.7) that the harmonic-like motion can persist for long times (on the relevant time-scale). Therefore, a curve fit to a harmonic solution minimising the residuals is applied to the deduced trajectory of the particle,

$$z(t) = z_0 \sin(\Omega_z t + \phi_0). \tag{6.29}$$

The fit generates the amplitude z_0 and phase offset ϕ_0. The fitted curve is then used to extrapolate the trajectory forward in time. Since the motion is expected to persist for long periods of time, the extrapolation is used to compensate for the computation time of the Kalman filter and curve fitting. The trap frequency Ω_z is assumed to be known as it is experimentally accessible. In the simulation, the frequency was found by fitting to the true particle trajectory. Results of fitting can be seen in figures (6.8) and (6.9). It can be seen in figure (6.8) that when a particle responds well to excitation it's position can generate a very accurate fit for all sample sizes, despite the lowest resolution consisting of only 24 points in a time window of 7.63μs. Figure (6.9) shows that a poorly-behaved particle trajectory can still be tracked especially at the highest resolution. For the lowest sample size, a small phase offset is introduced.

The turn-off time is found by considering points on a sine wave where the harmonic solution is zero and with positive gradient, as this is the point where the particle moves upwards with the highest velocity. Choosing the point of turn-off to be equidistant from the peak and the troth also ensures that the site hopping error due to a phase bias is minimal. Integer n is then chosen such that the rise point occurs after the final time step of the time window in which UKF is applied, with an integer N added to account for the computation time. Actual computation time of filtering and fitting was not used to deduce the value of N. Real computation time is too long and the resources were not available during the project to yield particle dynamics simulation tractable for that duration. Because of this, a far shorter, assumed computation time was used to obtain results. A condition on the value z_0 is required as the curve fit sometimes finds a negative value

of the amplitude which simply corresponds to a shift in the sine wave by π.

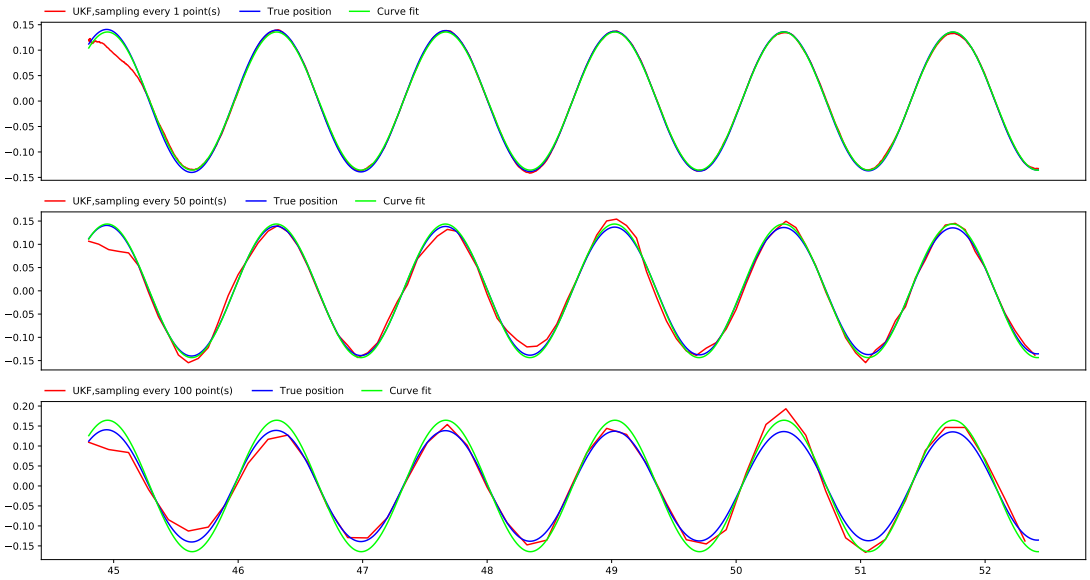

Figure 6.8: Position z in µm against time in µs. Filtering and curve fitting over a narrow time window of a well-behaved trajectory. The signal consists of 4768 points in the highest resolution case for a period of 7.63µs

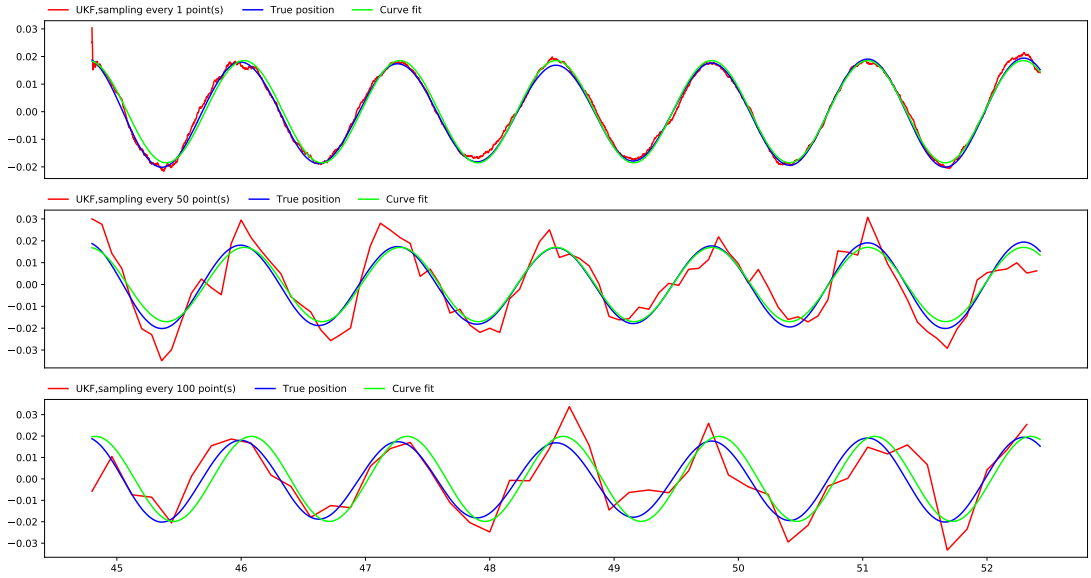

Figure 6.9: Position z in µm against time in µs. Filtering and curve fitting over a narrow time window of a badly-behaved trajectory. The signal consists of 4768 points in the highest resolution case for a period of 7.63µs

The modified algorithm aiming to transfer the particle one site *forward in the positive direction* can be summarised as follows:

1. Allow the simulated particles to thermalise or initiate a thermalised data set, after which turn on $M(t)$.

2. Parametrically excite the particles' motion for time t_{ex} using the sinusoidal function $M(t) = 1 + \beta \sin(\Omega_m t)$ where Ω_m is the modulation frequency.

3. Apply the Unscented Kalman filter to a time window of duration T_{UKF} and fit the deduced trajectory to a harmonic solution in equation (6.29).

4. Use the fitted parameters z_0 and ϕ_0 to deduce suitable values of T (the time at which the laser should be switch off) and τ (duration for which the laser should remain switched off). The turn-off time are found using,

$$T = \begin{cases} \frac{2n\pi - \phi_0}{\Omega_z} & \text{if} \quad z_0 > 0, \\ \frac{(2n+1)\pi - \phi_0}{\Omega_z} & \text{if} \quad z_0 < 0, \end{cases} \tag{6.30}$$

   where,*

$$n = \text{ceil}\left(\frac{\Omega_z t_f + \phi_0}{2\pi}\right) + N, \tag{6.31}$$

   t_f is the final time step before UKF is applied and N is an integer which encodes the computation time. The duration for which the laser is switched off is found using,

$$\tau = \frac{D_{\text{site}}}{\max(v_z)}, \tag{6.32}$$

   where D_{site} is the site separation (in the project $D_{\text{site}} \approx 0.75\mu\text{m}$) and $\max(v_z)$ is the maximum particle velocity in the z direction inferred using the UKF.

5. After time T, turn the laser off for a duration of τ. Equivalently, $M(t) = 0$ for $T \leq t < T + \tau$.

6. After time τ turn the laser back to normal mode of operation; $M(t \geq T + \tau) = 1$ to let the particles thermalise.

*'ceil' denotes a function which always rounds the number up to the next integer e.g. $2.4 \mapsto 3$.

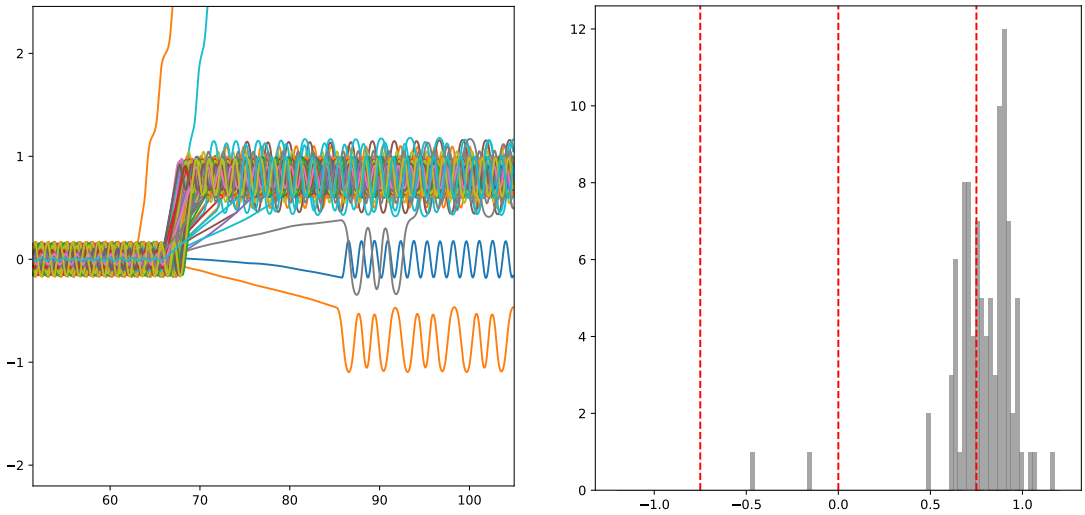

Figure 6.10: Application of the modified site hopping algorithm to 100 particle trajectories with the excitation parameter set to $\beta = 0.2$, $N = 10$ and maximum sampling resolution. (Left) Axial position in µm against time in µs. (Right) The corresponding histogram of axial position at the final time slice (displayed in a range -1.2µm $\leq z \leq$ 1.2µm for clarity) against the number of particles. The red bars show the approximate locations of intensity maxima sites. Two points are not displayed as they were located outside the specified range. The transfer successfully transferred 96% of particles.

Figures (6.10) and (6.11) show the results of using the modified algorithm for different values of N. Whilst almost perfect accuracy in the case of $N = 10$, the results show that the delay between computing the fit and release time has a drastic effect on the accuracy. The technique seems to lose its accuracy very quickly. It seems to be caused by the mismatch in between the particle's velocity upon release relative to the maximum velocity that the particle during the application of the filter. The method for selecting the value of τ is rather simplistic, assuming constant velocity and does not account for the particle possibly slowing down upon release. However, the method for selecting the release time T seems to be particularly effective, as in both cases few to no particles are released in the opposite direction. This is highly beneficial, since even if transfer was unsuccessful, the particle most likely remains in its current site and the transfer procedure can be repeated. This is also the case in figure (6.12), in which a 100 samples were sampled per microsecond. The figure shows similar performance to figure (6.11). In both cases the decrease in performance is caused by the poor velocity control; the particle either stays in the centre site because the laser is turned back on too soon or the particle is too fast after a successful transfer. This suggests that the simplistic approach of determining an appropriate value of τ could yield a much greater accuracy, if revised.

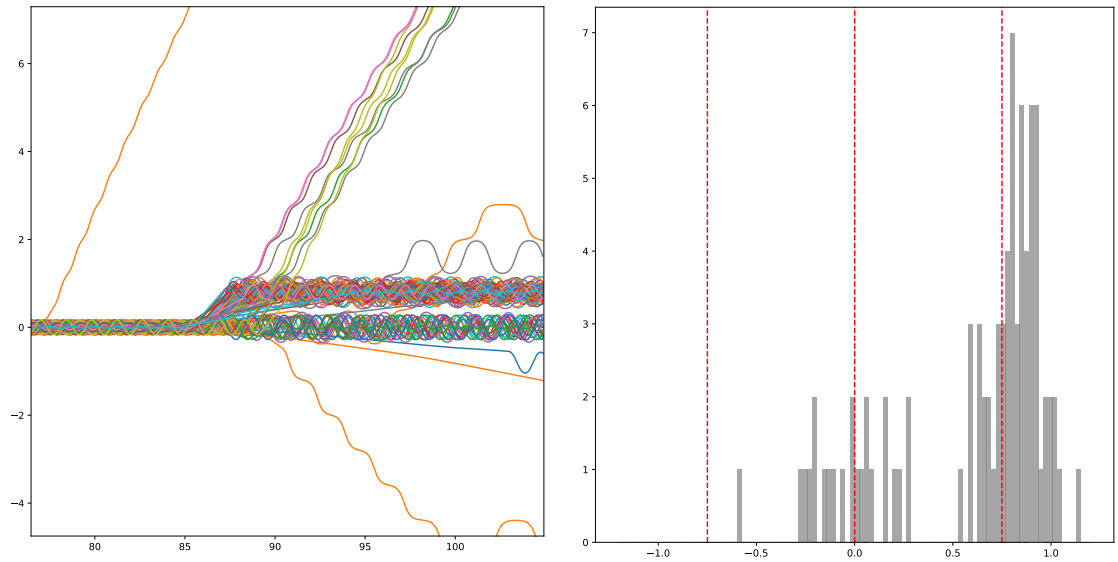

Figure 6.11: Application of the modified site hopping algorithm to 100 particle trajectories with the excitation parameter set to $\beta = 0.2$, $N = 25$ and maximum sampling resolution. (Left) Axial position in μm against time in μs. (Right) The corresponding histogram of axial position at the final time slice (displayed in a range -1.2μm $\leq z \leq$ 1.2μm for clarity) against the number of particles. The red bars show the approximate locations of intensity maxima sites. About 10 points are not displayed as they were located outside the specified range. The transfer successfully transferred 62% of particles.

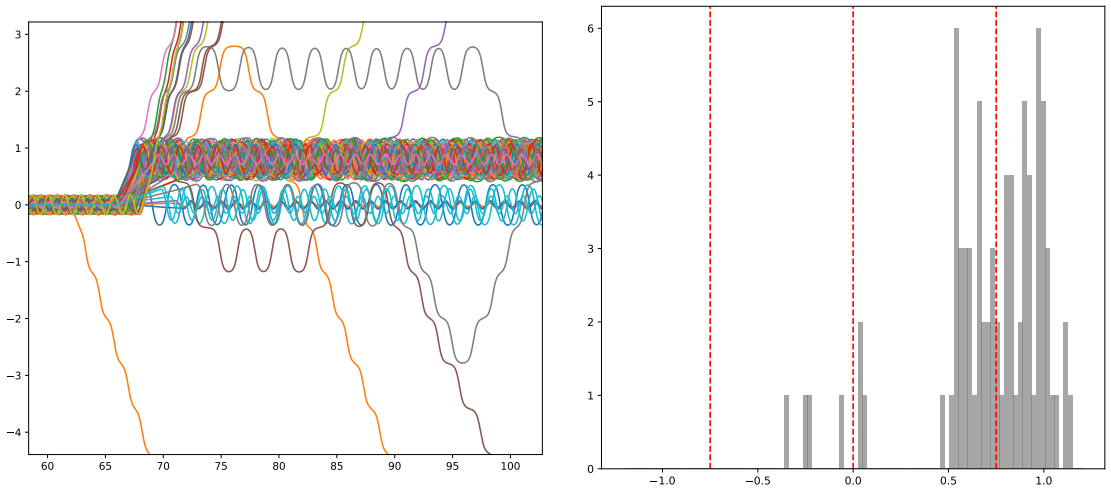

Figure 6.12: Application of the modified site hopping algorithm to 100 particle trajectories with the excitation parameter set to $\beta = 0.2$, $N = 25$ and sampling 100 points per μs. (Left) Axial position in μm against time in μs. (Right) The corresponding histogram of axial position at the final time slice (displayed in a range -1.2μm $\leq z \leq$ 1.2μm for clarity) against the number of particles. The red bars show the approximate locations of intensity maxima sites. Many points are not displayed as they were located outside the specified range. The transfer successfully transferred 64% of particles.

6.4 Experimental Considerations

As mentioned in the Introduction, the particle is to be stimulated to transfer between maxima of a standing wave by modulating the intensity of the beam. The stimulation can be achieved experimentally using an acousto-optic modulator whose driving RF signal modulates how much light is collected from the first-order diffraction beam. Modulating the signal can be done quickly in comparison to the time scales particle dynamics within the trap (Ω_z^{-1}) and the RF signal generator driving the AOM can accept complicated waveforms. Hence, this scheme provides a high degree of control over the gradient force acting on the particle.

Experimental application of the method requires careful consideration. The following four points have been identified as the main issues in the experimental implementation of the site hopping technique.

- **Computation time -** If filtering and fitting cannot be computed fast enough, the small errors due to frequency mismatch and phase offsets will build up and spoil the inferred knowledge of particle's position and velocity. The inference process and fitting took between a few milliseconds for the lowest sampling resolution to a few seconds for the largest sampling resolution using a Python implementation (code provided in the Appendix section 8.3). The particle is expected to behave harmonically for a time $\Gamma^{-1} = 20\mu s$ for 50kHz, such that the filter's dynamics are able to describe its motion. Although figure (6.7) shows that the harmonic motion can persist for far longer times, in both resolution cases the computation time is still far too long. Figure (6.11) shows that the accuracy depreciated very quickly after only about 20µs of assumed computation time. This makes the computation time one of the key limitations to implementing this site hopping technique in an experiment.

  In order to effectively mitigate the detriment to accuracy, computation time has to be reduced. An improvement to speed can be incorporated through the choice of the hardware architecture for the purpose of data acquisition and processing. One possible choice of a platform is a field-programmable gate array (FPGA). It is a form of reconfigurable computing architecture, bringing together the flexiblity of software and high performance of hardware. They contain an array of logic blocks which can be programmed together to implement complex algorithms with optimal gate usage and minimum input output latency. The filter can be programmed specifically for the purpose of implementing the site hopping scheme. However this can be a difficult task as it requires knowledge of digital circuit design and a hardware description language such as VHDL. A simpler and cheap alternative is perhaps a programmable system on a chip (PSoC) - this would involve some form of visual programming for configuration of the microcontrollers's pins

- **Relying on experimentally accessible parameters -** Results shown in the previous section were obtained under the assumption that a few key parameters were known due to their experimental accessibility. Knowledge of of the trap frequency Ω_z and damping rate Γ is necessary for Kalman filter input to model the system dynamics. A discrepancy in frequency would lead to a drift in the curve-fitted trajectory leading to a rapid loss of accuracy. However, both of these quantities can be observed by inspecting the power spectral density of the homodyne signal.

- **Initialisation -** Knowledge of initial position and phase was also assumed. The simulations were conveniently initialised with initial values of position and phase set to or close to their true values with low uncertainty encoded in the covariance. This had to be done because poor knowledge of the initial state yielded poor performance of the filter and in many cases divergence. A choice of initial position is less significant. Although it is required to even decide which direction of transfer to choose, the knowledge of which site the particle is located is sufficient (100nm resolution). The filter can then initiated with an underestimated uncertainty to avoid divergence, which would result a global phase offset in the trajectory, but the direction of travel and velocity could still be inferred. Analysis of the PSD could possibly be used as an initial position estimate through estimation of the average square position $\langle z^2 \rangle$.

  Poor choice of phase and high uncertainty leads to much more severe consequences; The filter diverges frequently and global phase offsets are common. Both of these effects lead to an extreme loss of accuracy. Initial phase can perhaps be obtained through its measurement before filtering. The phase is slowly drifting and varying significantly on the order of a minute ($\gamma^{-1} = 10$s), hence observing the power signal on this time scale could allow to deduce a suitable initial value for the phase. Alternatively, a lock-in amplifier could be used to measure the phase if the hardware is available and the reference signal is stable.

- **Measurement noise -** Measurement covariance $\mathbf{R} = 0.1^2$ in the simulation could be considerably higher compared with the $5.2\text{pW}/\sqrt{\text{Hz}}$ noise equivalent power of the `HCA-S-200M` photodiode used in the experiment. However, other sources of noise could be at play such as laser intensity fluctuations which increase the noise in the measurement. The signal is also likely to be lower than anticipated in section (5.4) due to misalignment of the optics or discrepancy introduced by the paraxial approximation which was used to obtain the estimate for a high NA lens. The Kalman filter performance is highly sensitive to the measurement noise and its performance depends on it. Therefore, any experimental means of decreasing it is an important factor when aiming to increase the accuracy of site hopping technique. All results were obtained with the excitation parameter set to $\beta = 0.3$. Increasing the excitation amplitude could have the effect of increasing the signal-to-noise ratio but could also have an effect on the velocity control.

7 Conclusions and Future Work

The main focus of the project was put on developing the site hopping scheme. The results presented show that, in principle, the scheme has a potential of achieving over 90% accuracy in transferring a particle to a desired site. At lower sampling resolutions, the scheme is still able to transfer more than 60% of particles, with the other particles remaining in its current site or leaving after a successful transfer. This indicates that better velocity control and estimation is required, which could lead to a dramatic increase in accuracy. Negligible number of particles in the study were transferred to the wrong site in all sampling cases, meaning that the technique could be re-applied to attempt another transfer after one that was unsuccessful.

The technique shows experimental promise, as the hardware required to implement it fast enough is available. Implementation on this hardware however would be a difficult task. The unscented Kalman filter is a recent analysis technique and its obscure application is unlikely to have available libraries or support on the hardware identified in section 6.4. It would need to be implemented from scratch, along with all of its numerical intricacies which ensure that the filter does not diverge during operation. In experimental application, the largest obstacle to overcome would be the estimation of the initial state. The user would need the knowledge of which site the particle resides in for a successful application which assures that the filter does not diverge. Further study of the occurrence of divergence could be beneficial. For example, limits could be placed on the maximum uncertainty 'allowed' by the filter without divergence.

8 Appendix

8.1 The Euler-Maruyama Method

For a stochastic differential equation,

$$dX_t = a(X_t)dt + b(X_t)dW_t, \tag{8.1}$$

where W_t and the initial condition $X_0 = x_0$, is a *Weiner process* the Euler-Maruyama method provides means of obtaining a numerical approximation of the true solution X_t for some interval $[0, T]$. The approximate solution is the Markov chain Y defined as follows:

1. Set $Y_0 = x_0$
2. Recursively define $\mathrm{Y}_{n+1} = Y_n + a(Y_n)\Delta t + b(Y_n)\Delta W_t$ where $\Delta t = T/N$ for N points τ_n in the interval $[0, T]$ and $\Delta W_t = W_{\tau_{n+1}} - W_{\tau_{n+1}}$.

ΔW_n has characterstic Weiner process properties; It is independent from $\Delta W_{n'}$ where $n \neq n^{'}$ and it is normally distributed about 0 with variance equal to Δt.

8.2 Particle Dynamics Code

```
#!/usr/bin/python3
import sys
import numpy as np
from numpy import pi, sqrt, exp, arctan, sin
from numpy.random import randn
from scipy.constants import c, epsilon_0, Boltzmann, g

def Modulation(t, turnoff):
    """ Intensity modulation function"""
    T1 = turnoff[0]
    T2 = turnoff[1]
    if t < 20e-6:
        return 1
    elif t < float(tchoice)*1e-6:
        return (1+beta*sin(Omega_Mod*t))
    elif t < T1:
        return 1
    elif t < (T1+T2):
        return 0
    else:
```

```
        return 1

def sde(f, x0, t_off, dt, dW):
    """Euler--Maruyama method for Stochastic Differential Equations"""
    tn = therm_t[-1]
    xn = x0
    sqrtdt = sqrt(dt)
    while True:
        yield tn,xn
        xn = xn + f(tn,xn,t_off)*dt + dW(sqrtdt)
        tn = tn + dt

def dW(sqrtdt):
    ans = np.zeros((N,6))
    ans[:,3:6] = dW0*randn(N,3)*sqrtdt
    return ans

def I(t,X,t_off):
    """Intensity as a function time and state vector.
    Expected to be separable into M(t)*I(x,y,z) and no dependence on vx,vy,vz."""
    x,y,z = X[:,0],X[:,1],X[:,2]
    r2 = x**2 + y**2
    w2 = w0**2*(1+(z/zR)**2)
    w = sqrt(w2)
    R = z*(1+(zR/z)**2)
    phi = arctan(z/zR)
    E1 = (w0/w)*exp(-r2/w2)*exp(-1j*( k*z + k*r2/(2*R) - phi))
    E2 = (w0/w)*exp(-r2/w2)*exp(-1j*(-k*z - k*r2/(2*R) + phi))
    Et = E1 + E2
    I = I0*abs(Et)**2
    M = np.array([Modulation(t, i) for i in t_off])
    return M*I

def gradI(t,X,t_off):
    """Forward difference numerical approximation to derivative of intensity I(t,X)"""
    I_centre = I(t,X,t_off)
    X_x = X.copy(); X_x[:,0] += delta
    X_y = X.copy(); X_y[:,1] += delta
    X_z = X.copy(); X_z[:,2] += delta
    I_x = I(t,X_x,t_off)
    I_y = I(t,X_y,t_off)
    I_z = I(t,X_z,t_off)
    ans = np.zeros((len(X),3))
    ans[:,0] = (I_x-I_centre)/delta
    ans[:,1] = (I_y-I_centre)/delta
    ans[:,2] = (I_z-I_centre)/delta
    return ans
```

```
68
69  def ForceGrad(t,X,t_off):
70      """Optical gradient force"""
71      return chi/(2*c)*gradI(t,X,t_off)
72
73  def f(t,X,t_off):
74      Xdot = np.zeros_like(X)
75      Xdot[:,0:3] = X[:,3:6]
76      Xdot[:,3:6] = ForceGrad(t,X,t_off)/mass
77      Xdot[:,3] += -g      # acceleration due to gravity
78      return Xdot
79
80
81
82  beta = float(sys.argv[1])    # Choice of modulation beta param
83  tchoice = sys.argv[2]        # Choice of modulation excitation time
84
85  therm_x = np.load('thermalised-x.npy') # Thermalised x data
86  therm_t = np.load('thermalised-t.npy') # Thermalised t data
87
88
89  wavelength = 1550e-9               # Laser wavelength
90  opower = 2.0                       # Optical power
91  w0 = 2e-6                          # Beam waist
92  Gamma = 50e3                       # Damping rate of particle
93  temp = 300.                        # Temperature
94  radius = 100e-9                    # Particle radius
95  density = 2329.                    # Particle density
96  Omega_Mod = 2*pi*793e3*2           # Modulation frequency
97  epsilon = 2.25                     # Relative permitivity
98  delta = 1e-9                       # Used for finite-difference approximation to spatial
        derivative
99  dt = 1e-10                         # Simulation time-step. Real time step approx. dt * 1e4
100 vol = (4/3)*pi*radius**3            # Particle volume
101 mass = density*vol                 # Particle mass
102 chi = 3*vol*(epsilon-1)/(epsilon+2) # The susceptibility
103 dW0 = sqrt(Gamma*Boltzmann*temp/mass) # Spread of the Weiner process
104 I0 = 2*opower/(pi*w0**2)           # Maximum laser intensity
105 zR = pi*w0**2/wavelength           # Rayleigh range
106 k = 2*pi/wavelength                # Wavenumber
107 N = 100                           # Number of particle trajectories
108
109 M = 2**19                         # Used later to generate the 1d time array
110 dM = 2**4
111
112 # Load thermalised data, if exists
113 from itertools import islice
```

```
if 'therm_x' in dir() and 'therm_t' in dir():
    print("Initialising thermalised data")
# Load release times and off durations for the trajectories
    T = np.load('offtimes.npy')
# Initial state = last state of thermalised data set
    X0 = therm_x[-1,:,:]
# Solve the DE using Euler-Maruyama
    solver = sde(f,X0,T,dt,dW)
    Xs = np.array([X for t,X in islice(solver, 0, M, dM)])
    ts = np.arange(therm_t[-1]/dt,M+therm_t[-1]/dt,dM)*dt
# Stick the thermalised data set and the evolved data set together
    Xs = np.vstack((therm_x,Xs))
    ts = np.append(therm_t,ts)
else:
    print("No thermalised data")
# Organise state-vector as (N particles) x (rx,ry,rz,vx,vy,vz) i.e. (N,6)
# Initialise particle positions at a random position within the centre site
# at zero velocity
    X0 = np.zeros((N,6))
    X0[:,0] = randn(N)*1e-9
    X0[:,1] = randn(N)*1e-9
    X0[:,2] = randn(N)*1e-9
    solver = sde(f,X0,dt,dW)
    Xs = np.array([X for t,X in islice(solver, 0, M, dM)])
    ts = np.arange(0,M,dM)*dt

np.save('x-b{}-t{}-m{}.npy'.format(bchoice,tchoice,ts[-1]),Xs)
np.save('tdata-{}.npy'.format(ts[-1]),ts)
```

8.3 Site Hopping Code

```
#!/usr/bin/python3
import numpy as np
import timeit
from scipy.optimize import curve_fit
from filterpy.kalman import UnscentedKalmanFilter as UKF
from filterpy.kalman import MerweScaledSigmaPoints
from filterpy.common import Q_discrete_white_noise
from filterpy.kalman import rts_smoother
from math import ceil

def sol1(t,a,w,b):
# For deducing true frequency
    return a*np.sin(w*t+b)

def sol2(t,a,b):
```

```
# Use known true frequency
    return a*np.sin(omega_z*t + b)

def F(state,dt):
# System dynamics
    F = np.array([[(C+(gamma/omega)*S)*E,S*E/omega,0,0],
                  [-S*E*omega_z**2/omega,(C-(gamma/omega)*S)*E,0,0],
                  [0,0, 1, (1-E2)/E2],
                  [0,0,0,E2]])
    return F @ state

def H(state):
# Measurement function
    z = state[0]
    theta = state[2]
    return (np.sin(kappa*z+theta),)

Xs = np.load('x-data.npy')[28000:,:,2]
ts = np.load('t-data.npy')[28000:]
theta = np.load('phase-data.npy')[28000:,:,0]
offtimes = np.zeros(Xs.shape[1]*2).reshape(Xs.shape[1],2)

gamma = 50e3                # Damping rate of position z
kappa = 4*np.pi/1550e-9     # Rate of change of phase with position z
gamma_phase = 0.1           # Damping rate of phase theta
sd = 0.1                    # Measurement noise standard deviation
sampling_every = 1          # Sample measurement every 1 point(s)
qvariance = 1e12            # Process noise of position and velocity
qvariance2 = 1e25           # Process noise of phase and its rate of change in time

t_sampled = ts[::sampling_every]
dt = (t_sampled[-1]-t_sampled[0])/len(t_sampled)

# Finding release time and off duration for all trajectories in Xs
for i in range(Xs.shape[1]):
# Deducing the true frequency using curve fitting, different for each trajectory
    T = ts[2000:]
    X = Xs[2000:,i]
    initials = [4e-8,4.85e6,0]
    p,cov = curve_fit(sol1,T,X,p0=initials)

    omega_z = p[1]
    omega = np.sqrt(omega_z**2 - gamma**2)

    S = np.sin(omega*dt)
    C = np.cos(omega*dt)
    E = np.exp(-gamma*dt)
```

```
    E2 = np.exp(-gamma_phase*dt)

# Generating sigma points
    points = MerweScaledSigmaPoints(n=4, alpha=0.1, beta=2., kappa=-1)
# Initiating the filter
    ukf = UKF(dim_x=4, dim_z=1, fx=F, hx=H, dt=dt, points=points)
    ukf.x = np.array([0,0,0,0])*1e-6
    ukf.P *= 1e-13
    ukf.R = sd**2
    vals = Xs[::sampling_every,i].size
# Simulate measurements
    Zs = np.random.normal(np.sin(kappa*Xs[::sampling_every,i] + theta[::sampling_every,i]),sd,vals)
    st = timeit.default_timer()
    ukf.Q[:2,:2] = Q_discrete_white_noise(2, dt=dt, var=qvariance)
    ukf.Q[2:,2:] = Q_discrete_white_noise(2, dt=dt, var=qvariance2)
# Filtering
    xs, Ps = ukf.batch_filter(Zs)
# Curve Fitting
    mx = int(xs[:,0].size/2)
    mx = int(0.5*xs.shape[0])
    T = ts[::sampling_every][mx:]
    X = xs[:,0][mx:]
    sigma0 = Ps[:,0,0][mx:]
    initials = [4e-8,0]
    p,cov = curve_fit(sol2,T,X,p0=initials)
# Select release time
    N = ceil((omega_z*ts[-1]+p[1])/(2*np.pi)) + 10
    if p[0]>0:
        T1 = (2*N*np.pi - p[1])/omega_z
    else:
        T1 = ((2*N+1)*np.pi - p[1])/omega_z
# Select off duration
    T2 = 0.75e-6/np.max(xs[:,1])
    offtimes[i] = T1,T2
    print(i,T1,T2)
np.save('offtimes.npy',offtimes)
```

9 Acknowledgements

References

[1] P. Lebedew. Untersuchungen über die druckkräfte des lichtes. *Annalen der Physik*, 311(11):433–458, 1901.

[2] S. Abiko. Einstein's theories of the fluctuation and the thermal radiation: The first quantum theory through statistical thermodynamics. *Historia Scientiarum*, 10(2):130–147, nov 2000.

[3] A. Ashkin. Applications of laser radiation pressure. *Science*, 210:1081–1088, December 1980.

[4] A. Ashkin, J. M. Dziedzic, J. E. Bjorkholm, and Steven Chu. Observation of a single-beam gradient force optical trap for dielectric particles. *Opt. Lett.*, 11(5):288–290, May 1986.

[5] M. Yu. Tikhonov V.B. Braginskii, A.B. Manukin. Investigation of dissipative ponderomotive effects of electromagnetic radiation. *JETP*, 58(5):829, 1970.

[6] V. B. Braginskii and A. Borisovich Manukin. *Measurement of weak forces in physics experiments / V. B. Braginsky and A. B. Manukin ; edited by David H. Douglass.* University of Chicago Press Chicago, 1977.

[7] M. Aspelmeyer, T. J Kippenberg, and F. Marquardt. Cavity optomechanics. *Reviews of Modern Physics*, 86(4):1391, 2014.

[8] P. F. Cohadon, A. Heidmann, and M. Pinard. Cooling of a mirror by radiation pressure. *Phys. Rev. Lett.*, 83:3174–3177, Oct 1999.

[9] D. Bouwmeester. Sub-kelvin optical cooling of a micromechanical resonator. In *Frontiers in Optics 2007/Laser Science XXIII/Organic Materials and Devices for Displays and Energy Conversion*, page JWA3. Optical Society of America, 2007.

[10] A. Schliesser, P. Del'Haye, N. Nooshi, K. J. Vahala, and T. J. Kippenberg. Radiation pressure cooling of a micromechanical oscillator using dynamical backaction. *Phys. Rev. Lett.*, 97:243905, Dec 2006.

[11] J. D. Thompson, B. M. Zwickl, A. M. Jayich, Florian Marquardt, S. M. Girvin, and J. G.E. Harris. Strong dispersive coupling of a high-finesse cavity to a micromechanical membrane (nature (2008) 452, (72)). *Nature*, 452(7189), April 2008.

[12] I. Favero, S. Stapfner, D. Hunger, P. Paulitschke, J. Reichel, H. Lorenz, E. M. Weig, and K. Karrai. Fluctuating nanomechanical system in a high finesse optical microcavity. *Opt. Express*, 17(15):12813–12820, Jul ts.

[13] S. Bose, K. Jacobs, and P. L. Knight. Scheme to probe the decoherence of a macroscopic object. *Phys. Rev. A*, 59:3204–3210, May 1999.

[14] W. Marshall, Christoph S., R. Penrose, and D. Bouwmeester. Towards quantum superpositions of a mirror. *Phys. Rev. Lett.*, 91:130401, Sep 2003.

[15] J. Gieseler, B. Deutsch, R. Quidant, and L. Novotny. Subkelvin parametric feedback cooling of a laser-trapped nanoparticle. *Physical Review Letters*, 109(10):103603, 2012.

[16] N. Kiesel, F. Blaser, U. Delić, D. Grass, R. Kaltenbaek, and M. Aspelmeyer. Cavity cooling of an optically levitated submicron particle. *Proceedings of the National Academy of Sciences*, 110(35):14180–14185, 2013.

[17] D. E. Chang, C. A. Regal, S. B. Papp, D. J. Wilson, J. Ye, O. Painter, H. J. Kimble, and P. Zoller. Cavity opto-mechanics using an optically levitated nanosphere. *Proceedings of the National Academy of Sciences*, 107(3):1005–1010, 2010.

[18] U. Delić, D. Grass, M. Reisenbauer, T. Damm, M. Weitz, N. Kiesel, and M. Aspelmeyer. Levitated cavity optomechanics in high vacuum. *Quantum Science and Technology*, 5(2):025006, mar 2020.

[19] J. Chan, T. Alegre, A. Safavi-Naeini, J. Hill, A. Krause, S. Groeblacher, M. Aspelmeyer, and O. Painter. Laser cooling of a nanomechanical oscillator into its quantum ground state. *Nature*, 478:89–92, 10 2011.

[20] Uroš Delić, Manuel Reisenbauer, Kahan Dare, David Grass, Vladan Vuletić, Nikolai Kiesel, and Markus Aspelmeyer. Cooling of a levitated nanoparticle to the motional quantum ground state. *Science*, 367(6480):892–895, 2020.

[21] G. Ranjit, M. Cunningham, K. Casey, and A. A. Geraci. Zeptonewton force sensing with nanospheres in an optical lattice. *Phys. Rev. A*, 93:053801, May 2016.

[22] V. Jain, J. Gieseler, C. Moritz, C. Dellago, R. Quidant, and L. Novotny. Direct measurement of photon recoil from a levitated nanoparticle. *Phys. Rev. Lett.*, 116:243601, Jun 2016.

[23] M. Motsch, M. Zeppenfeld, P. W. H. Pinkse, and G. Rempe. Cavity-enhanced rayleigh scattering. *New Journal of Physics*, 12(6):063022, jun 2010.

[24] G. Hétet, L. Slodička, A. Glätzle, M. Hennrich, and R. Blatt. Qed with a spherical mirror. *Phys. Rev. A*, 82:063812, Dec 2010.

[25] A. E. Siegman. *Lasers*. University Science Books, 1986.

[26] L. Novotny and B. Hecht. *Principles of nano-optics*. Cambridge University Press, 2006.

[27] C. J. Foot. *Atomic physics*. Oxford master series in atomic, optical and laser physics. Oxford University Press, Oxford, 2007.

[28] N. Khan, A. Hye, Md. R. R. Mojumdar, and S. Rahman. Behavior analysis of a gaussian beam optical trap in the rayleigh regime. 07 2012.

[29] Keir C. Neuman and Steven M. Block. Optical trapping. *Review of Scientific Instruments*, 75(9):2787–2809, 2004.

[30] H. Risken and H. Haken. *The Fokker-Planck Equation: Methods of Solution and Applications Second Edition*. Springer, 1989.

[31] C. Dawson and J. Bateman. Spectral analysis and parameter estimation in levitated optomechanics. *J. Opt. Soc. Am. B*, 36(6):1565–1573, Jun 2019.

[32] R. Grover Brown and P. Y. C. Hwang. *Introduction to random signals and applied kalman filtering: with MATLAB exercises and solutions; 3rd ed.* Wiley, New York, NY, 1997.

[33] E. A. Wan and R. Van Der Merwe. The unscented kalman filter for nonlinear estimation. 2000.

[34] S. J. Julier and J. K. Uhlmann. A new extension of the kalman filter to nonlinear systems. 1997.

[35] R. Labbe. Kalman and bayesian filters in python. `https://github.com/rlabbe/Kalman-and-Bayesian-Filters-in-Python`, 2014.

[36] H. J. R. Dutton. *Understanding Optical Communications*. IBM Corporation, International Technical Support Organization, U.S., 1998.

[37] L. Vecellio. The mesh nebuliser: a recent technical innovation for aerosol delivery. *Breathe*, 2:252–260, 2006.

[38] M. D. Summers, D. R. Burnham, and D. McGloin. Trapping solid aerosols with optical tweezers: A comparison between gas and liquid phase optical traps. *Opt. Express*, 16(11):7739–7747, May 2008.